Closed-Loop Long-Term Experimental Molecular Communication System

Maike Scherer⋆, Lukas Brand⋆, Louis Wolf, Teena tom Dieck, Maximilian Schäfer, Sebastian Lotter, Andreas Burkovski, Heinrich Sticht, Robert Schober, and Kathrin Castiglione

Friedrich-Alexander-Universität Erlangen-Nürnberg, Erlangen, Germany

Abstract

We present a fluid-based experimental molecular communication (MC) testbed which uses media modulation. Motivated by the natural human cardiovascular system, the testbed operates in a closed-loop tube system. The proposed system is designed to be biocompatible, resource-efficient, and controllable from outside the tube. As signaling molecule, the testbed employs the green fluorescent protein variant "Dreiklang" (GFPD). GFPDs can be reversibly switched via light of different wavelengths between a bright fluorescent state and a less fluorescent state. GFPDs in solution are filled into the testbed prior to the start of information transmission and remain there for an entire experiment. For information transmission, an optical transmitter (TX) and an optical eraser (EX), which are located outside the tube, are used to write and erase the information encoded in the state of the GFPDs, respectively. At the receiver (RX), the state of the GFPDs is read out by fluorescence detection. In our testbed, due to the closed-loop setup and the long experiment durations of up to 125 hours, we observe new forms of inter-symbol interferences (ISI), which do not occur in short experiments and open-loop systems. In particular, up to four different forms of ISI, namely channel ISI, inter-loop ISI, offset ISI, and permanent ISI, occur in the considered system. For the testbed, we developed a communication scheme, which includes blind transmission start detection, symbol-by-symbol synchronization, and adaptive threshold detection, that supports higher order modulation. We comprehensively analyze our MC experiments using the absolute mean Euclidean distance (AMED), eye diagram, and bit error rate (BER) as performance metrics. Furthermore, we experimentally demonstrate the error-free transmission of 5370 bit at a data rate of 36 $\mathrm{bit\,min^{-1}}$ using 8-ary modulation and the error-free binary transmission of around 90,000 bit at a data rate of 12 $\mathrm{bit\,min^{-1}}$. For the latter experiment, data was transmitted continuously for a period of more than five days (125 hours) during which no signaling molecules were injected into or removed from the system. All signals recorded during the experiments, representing more than 250 kbit of data transmitted via MC, and parts of the evaluation code are publicly available on Zenodo and Github, respectively.

I. INTRODUCTION

Synthetic molecular communication (MC) is an emerging research field at the intersection of biology, nanotechnology, and communications engineering. Inspired by natural processes, MC offers innovative methods to transmit information by encoding it into chemical signals [2]. This approach has the potential to enable transformative applications in medicine [3], [4], nanotechnology [5], [6], agriculture [7], and environmental monitoring [8] by providing

---

⋆ Co-first authors.

biocompatible and energy-efficient communication solutions, particularly in environments where conventional communication methods are impractical [9].

So far, most work in MC has focused on theoretical research, resulting in the development of theoretical models and communication schemes [9]–[12]. However, in order to advance from theory to the envisioned applications of MC, it is crucial to develop experimental testbeds to bridge the gap between theoretical concepts and their practical application [13]. In recent years, there has been a notable increase in experimental MC research and the number of experimental testbeds. A comprehensive overview on experimental MC is provided in [13], [14].

A significant portion of MC research has focused on medical applications, including in-body communication, health monitoring, and targeted drug delivery [3]. Consequently, suitable MC testbeds aim to model these application scenarios, e.g., MC within the human cardiovascular system, which directly influences their design. Therefore, many existing MC testbeds [15]–[21] try to emulate real-world conditions, e.g., by employing biocompatible signaling molecules and by mimicking relevant aspects of the closed-loop human cardiovascular system using tube-based propagation channels with a background fluid flow [14]. However, most existing testbeds are only partially successful in this regard. On the one hand, the testbeds presented in [15]–[17] use biocompatible signaling molecules – specifically, superparamagnetic iron-oxide nanoparticles (SPIONs), the cyanine dye indocyanine green, and the salt sodium chloride, respectively, that have the potential to be used in future *in vivo* applications. On the other hand, all previously mentioned testbeds [15]–[21] share the limitation of considering only simple topologies – primarily a single straight duct as the propagation channel – and lack self-containment, i.e., they operate as open-loop systems. Here, open-loop refers to systems where the background fluid used in the experiment can enter or leave the system during operation. As a result, in these testbeds, the signaling molecules are added to the tube system at one point, e.g., via an injection, are used *once* for information transmission, and then are collected as waste at the end of the tube. **Such systems have two major drawbacks**: First, long-term transmission experiments generate a lot of waste. Second, many of the intended applications target closed-loop environments, e.g., the human cardiovascular system, and cannot be accurately emulated by open-loop topologies.

Therefore, experimental MC systems are required where the communication system operates within a closed-loop tube system. Currently, there are only two MC testbeds operating in a closed-loop topology [22], [23]. In [22], a fluid is pumped in a closed-loop system while fluorescent particles are injected, detected, and then diluted. The testbed presented in [23] constitutes the first *in vivo* MC testbed and is based on the chorioallantoic membrane of fertilized chicken eggs, where the fluorescent dye indocyanine green is injected into a closed-loop vascular system. However, the repeated dilution of fluorescent particles in [22] reduces their detectability in long-term experiments, and in [23], only a single

injection is considered due to the strong soiling of the vascular system by indocyanine green molecules. Moreover, in both testbeds, the signaling molecules can be used only for a single transmission, which is not resource efficient. Therefore, although the testbeds in [22], [23] consider a closed loop, their applicability for long-term experiments is limited.

In this paper, we propose the first experimental closed-loop MC testbed in which reversibly switchable signaling molecules are reused multiple times, enabled by molecular *media modulation* [24]. In media modulation, signaling molecules with specific switching properties [25] are employed and, unlike in conventional MC systems, they are injected only once into the system. Then, the state of the signaling molecules is repeatedly switched to transmit information, i.e., no additional molecules are injected into or removed from the system during operation. Compared to common injection-based release mechanisms [13], in media modulation, the transmitter (TX) can be placed outside the MC channel and does not affect the propagation environment. As signaling molecule, we adopt the biocompatible green fluorescent protein variant "Dreiklang" (GFPD) [26], [27]. GFPDs can be reversibly switched between a bright fluorescent ON state and a less fluorescent OFF state via light stimuli of different wavelengths [27]. This allows for writing and erasing information employing an optical TX and eraser (EX), respectively. The state of the GFPDs, which conveys the transmitted information, is read out via fluorescence detection at the receiver (RX). In summary, the proposed MC testbed facilitates resource-efficient communication and long-term experiments, and significantly reduces channel soling. By considering a closed-loop propagation environment, the testbed mimics an important property of the cardiovascular system, and the use of the biocompatible signaling molecule GFPD ensures relevance for future applications.

In this paper, we provide a comprehensive description and analysis of the proposed closed-loop media modulation testbed, its construction, and its components. Moreover, we discuss the chemical properties of the biocompatible signaling molecule GFPD and their impact on communication performance. We identify three forms of inter-symbol interference (ISI), i.e., inter-loop ISI, offset ISI, and permanent ISI, which occur particularly in closed-loop systems and during long-term experiments based on media modulation, and propose methods for their mitigation. In addition, we develop and analyze a suitable communication scheme for the considered experimental MC system. Several communication schemes, including methods for modulation [12], [18], synchronization [28]–[31], as well as detection [21], [32], [33], have been developed for MC. In this paper, we desgin a communication scheme suitable for the proposed closed-loop media modulation testbed, building on the existing literature. In particular, the developed scheme comprises a noise estimation-based wake-up method, higher-order modulation, blind and data-based synchronization, and adaptive threshold-based detection. Although these methods are developed with a focus on the considered media modulation testbed, they can be generalized to other experimental MC

testbeds, as they are deliberately introduced in a general form. Furthermore, we discuss relevant qualitative and quantitative performance metrics for experimental MC systems, including bit error rate (BER), eye diagram, and absolute mean Euclidean distance (AMED), and apply these metrics to evaluate the performance of the developed communication scheme. Furthermore, we present the first long-term MC experiment, achieving error-free transmission of around $90,000$ bit sent over more than five days. This demonstrates the reliability of the proposed testbed and highlights the potential of media modulation-based MC as a promising approach for future applications, such as long-term health monitoring. Finally, we compare the proposed media modulation testbed to existing MC testbeds, in terms of communication-theoretical metrics such as the BER, molecule efficiency, and detection methods.

The main contributions of this paper can be summarized as follows:

- We utilize light-based media modulation to transmit information in a closed-loop tube system using the states of the biocompatible and reusable signaling molecule GFPD. This form of media modulation enables the operation of TX, EX, and RX outside of the tube. As a result, they do not interfere with the propagation of the signaling molecules inside the tube; a feature that is beneficial, e.g., for healthcare applications. By considering a closed-loop topology, we ensure that the proposed testbed resembles and allows to study an important property of the cardiovascular system.

- Because of the closed-loop and long experiments, new forms of ISI occur, which become apparent on different time scales. We characterize these forms of ISI and implement suitable ISI mitigation schemes.

- We develop a communication scheme for the considered system that can also be used in other experimental MC testbeds. The scheme includes a noise-estimation based wake-up method and data-based and blind synchronization. Furthermore, for detection, we propose an adaptive threshold detector. The transmission characteristics of the testbed are evaluated comprehensively - specifically by metrics such as AMED, eye diagrams, and BER.

- We experimentally demonstrate the error-free data transmission of $5,370$ bit at a data rate of $36\,\mathrm{bit\,min^{-1}}$, where 8-ary modulation is used. In addition, to the best of our knowledge, we report the longest MC experiment to date: Error-free transmission of around $90,000$ bit over a period of more than 5 consecutive days ($125\,\mathrm{h}$) at a data rate of $12\,\mathrm{bit\,min^{-1}}$. No molecules were injected into or extracted from the system during this time, i.e., only $9\,\mathrm{mL}$ of GFPD solution with a concentration of $C_{\mathrm{GFPD}} = 0.3\,\mathrm{mg\,mL^{-1}}$ were required for the entire experiment. By this, we demonstrate the superiority of media modulation for long MC experiments compared to the repeated injection of molecules employed in existing MC testbeds.

- All our experimental data (more than 250 kbit transmitted across different experimental

settings) as well as the Python code for evaluation have been released in open access [34]. This large amount of experimental data enables other researchers to develop and evaluate alternative processing methods for the received signals, e.g., machine learning based algorithms.

We note that a preliminary and simplified version of the testbed was briefly presented as part of [25]. In [25], the experiment duration was only 3 min, which did not allow to i) evaluate the resource efficiency of the testbed, ii) characterize the ISI, and iii) experimentally determine the BER for different detection schemes, which are new contributions of this work. Moreover, this paper significantly extends its conference version [1]: We extend the communication schemes developed in [1] by methods for synchronization, blind transmission start estimation, and adaptive threshold detection. Moreover, in this paper, we consider higher order modulation schemes, i.e., 8-ary modulation, and employ the AMED and eye diagrams as performance metrics to evaluate the transmission characteristics of the testbed. While in [1] the error free transmission of 500 bit for an experiment of duration 250 min was shown, in this paper, we consider the transmission of 90,000 bit for over 5 days.

The remainder of this paper is organized as follows. In Section II, we provide an overview of the proposed closed-loop testbed, including a detailed description of the signaling molecule GFPD, the testbed components, and the working principle of the testbed. We discuss the physical properties of the testbed and their influence on communication performance in Section III. In Section IV, we describe the proposed communication scheme in detail, including modulation, symbol synchronization, and detection. The proposed performance metrics are presented in Section V, and our results and evaluation are provided in Section VI, which we compare with results achieved with other testbeds in Section VII. Finally, Section VIII concludes the paper and outlines topics for future work.

II. TESTBED OVERVIEW

In this section, an overview of the testbed is provided. A schematic representation of the building blocks of the testbed and their functionality is displayed in Fig. 1a, while Fig. 1b shows the testbed during operation.

A. Closed-Loop System: Tube System and Pump

For our testbed, we use a fluorinated ethylene propylene (FEP) tube with radius $r_T = 8 \times 10^{-4}$ m and total length $L_T = 2.74$ m. To achieve the closed-loop structure, both ends of the tube are put into a test tube (*Falcon*®). The *Falcon*® is filled with $V_R = 2.50$ mL of fluid[1]. Hence, as long as both ends of the tube are immersed in the fluid of the *Falcon*®, they are hereby connected. To ensure this, $V_R = 2.50$ mL are suitable to immerse the tube ends in the fluid even if the tubes move slightly during the pumping process.

---

[1]In fact, the fluid is a solution of dissolved GFPD. Details on the composition of the GFPD solution and its introduction into the system are provided in Section II-C.
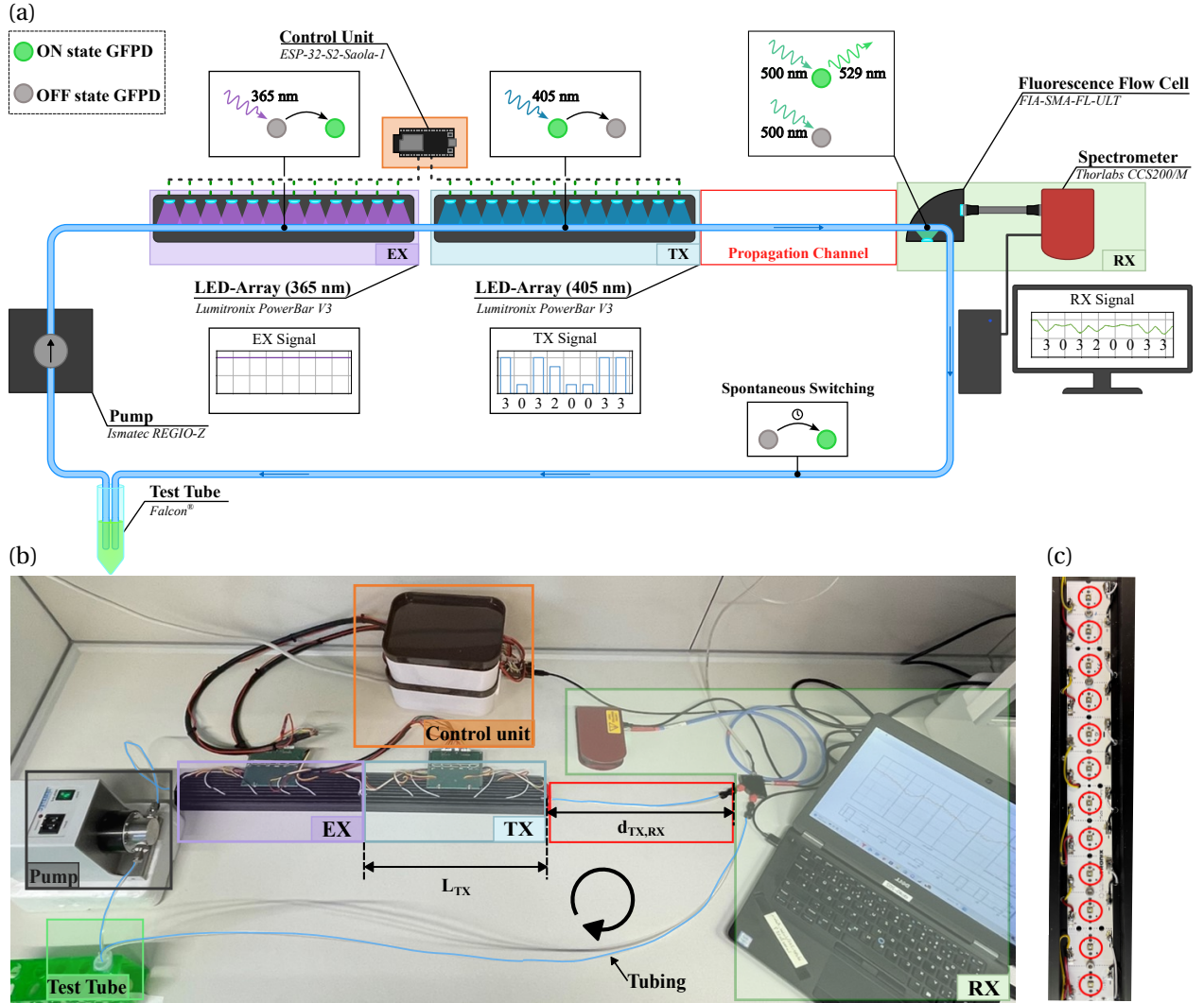
Figure 1. (a) Schematic representation of the testbed consisting of the propagation channel, pump, test tube, two LED-arrays serving as TX and EX, respectively, a flow cell, and a spectrometer acting as RX. The switching processes of GFPD are depicted next to the components in which they occur. (b) Photo of the experimental setup during operation. (c) LED array of the TX module (the LED module of the EX looks similar). Individual LEDs of the array are highlighted by red circles.

For pumping, a gear pump (*Ismatec REGLO-Z*), attached to the tube, is used. The pump drives the fluid in the system with an effective volume flux of $Q = 9.45\,\mathrm{mL\,min^{-1}}$, leading to an effective flow velocity of $v_{\mathrm{eff}} = 0.139\,\mathrm{m\,s^{-1}}$ for the given radius of the tube r_{T}.

B. Signaling Molecule: GFPD and Its Properties

GFPD is a photoswitchable and biocompatible green fluorescent protein (GFP) introduced in [27]. The authors in [27] show that GFPD has some unique properties, which make it well suited for the use in our testbed. In particular, the switching efficiency, robustness to photobleaching, and fluorescence intensity are high for GFPD. In the following, we discuss these properties of GFPD in detail.

1) Reversible Photoswitchability – Modulation und Resetting via Active Switching: In general, *photoswitchability* means that the properties of a molecule can be changed upon exposure to light of specific wavelengths. In the case of GFPD, photoswitchability allows for a reversible

switching of its fluorescence between two[2] distinct states, namely the ON and OFF states, which can be controlled by irradiation of light with different wavelengths. In particular, GFPD may be switched to the ON and OFF states upon irradiation with light of wavelengths $\lambda_{\mathrm{ON}} = 365\,\mathrm{nm}$ and $\lambda_{\mathrm{OFF}} = 405\,\mathrm{nm}$, respectively. The success of the switching depends on the intensity of the irradiation. The switching property allows the modulation and deletion of information into and from the state of the GFPD, facilitated by a TX and EX module in our testbed, respectively, which are discussed in detail in Section II-D.

2) Fluorescence-Based State Readout: Only GFPDs in the ON state show a high fluorescence, i.e., emit light at a wavelength of $\lambda_{\mathrm{E}} = 529\,\mathrm{nm}$ after being excited by light of wavelength $\lambda_{\mathrm{T}} = 500\,\mathrm{nm}$. Hence, the wavelengths responsible for switching, i.e., 365 nm and 405 nm, are decoupled from the fluorescence excitation and detection wavelengths. To read the fluorescence, we use a spectrometer in our testbed, which is detailed in Section II-D.

3) Thermal Relaxation to the ON State: Thermal relaxation denotes the process by which a perturbed system spontaneously returns to its equilibrium state. For GFPD, this means that an OFF state GFPD can spontaneously switch back to its ON state. The thermal relaxation of GFPD to the ON state has a half-life of $T_{1/2} = 600\,\mathrm{s}$ at room temperature [27]. As the thermal relaxation process depends on temperature, a laboratory with constant room temperature, 21°C in our case, supports reproducible experimental results.

We note that only the ON state of GFPD is thermodynamically stable [27]. Consequently, the ON state is predominant in equilibrium in the proposed testbed.

4) High Robustness to Photobleaching: After multiple photoswitching cycles and readouts, photobleaching of GFPD may occur [27]. Photobleaching is a general phenomenon when irradiating GFP and its variants such as GFPD and refers to the rare event of destruction of the fluorophore molecule upon exposure to light. Photobleaching is energy dependent, i.e., it increases with higher irradiation power or longer irradiation duration [27, Suppl. Fig. 7]. A photobleached GFPD irreversibly loses its ability to be fluorescent [27], [35], which can be interpreted as GFPD degradation, visible as a gradual decrease of fluorescence intensity upon repeated exposure to light.

5) Biocompatibility: Like all GFPs, GFPD is *biocompatible* [26]. This property allows the use of GFP-based proteins in a wide range of living organisms without causing significant harm or disruption to their normal functions [26]. The biocompatibility of GFPD also makes our laboratory experiments safe.

C. Experimental Procedure

Before the testbed can be used for information transmission, the GFPD solution must be prepared and filled into the testbed. Hence, each experiment involves the following steps.

---

[2]In fact, a third state exists, which we denote as *equilibrium state*. In the absence of light, GFPD may switch to this state, which shows a fluorescence similar to that of the ON state. As the equilibrium state's fluorescence is only slightly higher, in this work, for simplicity of presentation, we do not differentiate between the ON state and the equilibrium state.

1) Step 1 (Preparation of GFPD Solution): Phosphate-buffered saline (PBS) buffer, a water-based salt solution, is used as the liquid buffer medium. Specifically, a high-concentration stock of GFPD is diluted with PBS buffer and the detergent Triton X-100, which is also needed to stabilize GFPD for long-term experiments, to a total volume of $9\,\mathrm{mL}$. In the end, the GFPD solution contains a GFPD concentration of $C_{\mathrm{GFPD}} = 0.3\,\mathrm{mg\,mL^{-1}}$ and a Triton X-100 concentration of $C_{\mathrm{TRITON}} = 0.125\,\mathrm{mg\,mL^{-1}}$.

2) Step 2 (Filling the GFPD Solution into the Closed-Loop System): The GFPD solution is pumped into the tube, which has a volume of $V_{\mathrm{T}} = 5.43\,\mathrm{mL}$, and all segments within the pump and flow cell, which have a joint volume of $V_{\mathrm{PF}} = 1.07\,\mathrm{mL}$, until the test tube is filled with $V_{\mathrm{R}} = 2.50\,\mathrm{mL}$, which requires in total $9\,\mathrm{mL}$ of GFPD solution. At this point, both ends of the tubing are placed in the test tube to close the loop.

3) Step 3 (Information Transmission): While the pump constantly transports the GFPD solution in the loop, information can be modulated from outside the tube into the state of the GFPDs by an LED-based TX. Later, the RX reads out the state of the GFPDs via fluorescence triggered by an LED. Additionally, an LED-based EX can be used to erase the modulated information. Note that the average lap time that one GFPD molecule needs to circulate one time through the testbed is $T_{\mathrm{L}} = \frac{V_{\mathrm{PF}} + V_{\mathrm{T}}}{Q} = 41\,\mathrm{s}$ assuming, on average, no additional delay is induced by the *Falcon®*. The components that facilitate information transmission, i.e., the TX, the TX-RX link, which we refer to as channel, the RX, and the EX are described next.

D. Information Transmission Components

1) The Transmitter - Optical-to-Chemical-Signal Conversion: The TX is used to modulate information via media modulation into the state of the GFPDs. Since the ON state is the idle state of the GFPDs, the TX switches GFPD to the OFF state to convey information. The TX consists of an LED array with 12 equally spaced LEDs (*PowerBar V3, Lumitronix*), cf. Fig. 1c, which can emit light at a wavelength of $\lambda_{\mathrm{OFF}} = 405\,\mathrm{nm}$. The array is attached to an aluminum circuit board with a total length of $L_{\mathrm{TX}} = 29\,\mathrm{cm}$ that is connected to a passive cooling element to increase the service life of the LEDs. In addition, the LEDs are individually wired for maximum flexibility. This design enables control of the irradiation intensity of each LED by a microcontroller (*ESP32-S2, Espressif Systems*) during the experiments. In this work, however, all LEDs are switched on and off simultaneously. The TX is placed on top of the tubing, cf. Fig. 1.

To encode information, the TX emits light for a duration of T_{I} and hereby controls the ON state concentration of the irradiated GFPD molecules in the tubing. The irradiation intensity is adapted according to the symbol to be transmitted (cf. Section IV-A for mathematical details). The switching of GFPD is an energy-dependent probabilistic process [24], [27]. In our testbed, both the irradiation duration T_{I} and the irradiation intensity jointly determine

the switching probability. This is because both determine the total number of photons released during T_I, which in turn determines the probability that a photon will hit a GFPD molecule and thus trigger a switch. T_I is followed by a guard interval of duration T_G, during which the TX is always inactive. This results in a symbol duration of $T_S = T_I + T_G$.

2) The Channel - Pump-Driven Advection: In the testbed, information is transmitted over the communication channel of length $d_{TX,RX}$, which we define to be the tubing between the end of the TX and the beginning of the RX (framed in red in Figs. 1a and 1b). In this work, two channel lengths are investigated, $d_{TX,RX} = 6\,cm$ and $d_{TX,RX} = 35\,cm$. Note that our testbed design allows for easy modification of $d_{TX,RX}$ by moving the TX, which is loosely placed on top of the tube. In principle, $d_{TX,RX}$ could even be varied dynamically during experiments. In this work, however, the TX is not moved during experiments.

During the propagation from the TX to the RX, modulated GFPD molecules may spontaneously switch back to their ON state due to thermal relaxation. In our experiments, the effect on the received signal is small as $T_{1/2} = 600\,s$ is large compared to the average time required to propagate the distance $d_{TX,RX}$ (0.4 s and 2.5 s for $d_{TX,RX} = 6\,cm$ and $d_{TX,RX} = 35\,cm$, respectively, assuming $v_{eff} = 0.139\,m\,s^{-1}$). However, for future experiments with a longer channel, thermal relaxation may become more relevant.

3) The Receiver - Fluorescence-Based Readout: The RX is used to read out the current states of the GFPDs. As RX, a fluorescence flow cell (*FIA-SMA-FL-ULT, Ocean Optics*), equipped with an LED that can emit light at a wavelength of $\lambda_T = 500\,nm$, is placed at a distance of $d_{TX,RX}$ from the end of the TX. The LED is used to trigger the fluorescence of the GFPD. The light emitted by the GFPDs upon fluorescence, which has a wavelength of $\lambda_E = 529\,nm$, is guided by an optical fiber and measured by a compact spectrometer (*CCS 100M, Thorlabs*). The measured signal is recorded by the *ThorSpectra software*.

4) The Eraser - Deleting the Modulated Information: The EX can be used to reset the state of the GFPDs to the ON state. The EX consists of an LED array with 12 equally spaced LEDs (*PowerBar V3, Lumitronix*), which can emit light at a wavelength of $\lambda_{ON} = 365\,nm$. Apart from the type of LEDs used, the EX is constructed and wired identical to the TX, i.e., the hardware design and dimensions of the EX are identical to those of the TX. The EX is placed upstream next to the TX.

Compared to the TX, the use of the EX is optional. Consequently, two scenarios are considered: one with and one without the use of the EX. In the case without EX, GFPD can only switch back from the OFF state to the ON state by thermal relaxation. If we use the EX, the EX is turned on at the beginning of the experiment, i.e., the EX is continuously active. Hence, the EX enables the active reset of the GFPDs from the OFF state back to the ON state. In consequence, with the EX turned on, the number of ON state molecules available at the TX is increased. In addition, the EX effectively reduces memory effects in the system, i.e., it can be used to reduce the forms of ISI specific to closed-loop MC systems. We will

discuss these forms of ISI in detail in Section III-B. As a side effect, the EX also contributes to photobleaching, cf. Section II-B4. Thus, the use of the EX causes a tradeoff between ISI mitigation and additional photobleaching.

III. Physical Characterization of the Testbed

In this section, we discuss the physical effects observed in the testbed, such as the involved fluid mechanics and different forms of ISI present including those that occur exclusively in closed-loop systems.

A. Signaling Molecule Propagation

In our testbed, the propagation of the GFPD signaling molecules is mainly affected by advection, facilitated by the bulk background flow of the buffer liquid. In the following, we analyze the flow characteristics and its parameters in the testbed.

When a fluid of kinematic viscosity ν flows with average flow speed v_{eff} through a pipe of radius r_{T}, either laminar flow or turbulent flow occurs. Which type of flow is dominant can be predicted by the Reynolds number $\mathrm{Re} = \frac{2 r_{\mathrm{T}} v_{\mathrm{eff}}}{\nu}$ [36, p. 14]. For increasing Reynolds numbers, the transition from the laminar to the turbulent flow regime occurs around $\mathrm{Re} \approx 2300$ [37, p. 12]. The viscosity of the buffer solution in our testbed equals the viscosity of water [38], i.e., $\nu = 1.037 \times 10^{-6}\,\mathrm{m^2\,s^{-1}}$ (at 21 °C). Here, for the parameter regime in which the testbed is operated, we obtain $\mathrm{Re} = 167$, i.e., laminar flow is dominant. This value of Re corresponds to a medium-sized artery, where the Reynolds number is typically between 100 and 1000 [39]. Furthermore, we determine the relative influence of diffusion on the fluid transport, which can be characterized by the dimensionless Péclet number $\mathrm{Pe} = \frac{r_{\mathrm{T}} v_{\mathrm{eff}}}{D}$ [40, eq. (4.44)]. Here, utilizing the diffusion coefficient $D = 1 \times 10^{-10}\,\mathrm{m^2\,s^{-1}}$ of GFPD [41], $\mathrm{Pe} = 1.11 \times 10^{6} \gg 1$ follows. Therefore, flow dominates over diffusion in the system, and the latter can be neglected as a result.

B. ISI Caused by Closed-Loop Operation

The closed-loop character of our testbed gives rise to four distinct forms of ISI: *channel ISI*, *inter-loop ISI*, *offset ISI*, and *permanent ISI*. The latter three forms can only be observed in closed-loop systems. All forms of ISI are discussed in detail in the following.

1) Channel ISI: Within the channel, the propagation of OFF state GFPD molecules from TX to RX may result in the overlap of consecutive transmitted symbols, leading to ISI. The existence of channel ISI has been demonstrated with existing MC testbeds, e.g., [17], [42]. Channel ISI can be mitigated by introducing a guard interval T_{G}, during which the TX is inactive, where the effectiveness of ISI mitigation is contingent on the duration of the guard interval. However, increasing T_{G} also results in a reduction of the achievable data rate.

2) Inter-Loop ISI: Due to the closed-loop design of the testbed, inter-loop ISI occurs, as the OFF state GFPD molecules remain in the system and reenter the RX after completing one loop. Hence, these molecules interfere not only with neighboring symbols (as is the case for channel ISI) but also with symbols transmitted much later in time. In particular, OFF state GFPD molecules, which are switched to the OFF state by the TX, may travel several times through the loop before they spontaneously switch back to the ON state. Thus, these signaling molecules are likely to affect the received signal multiple times, while the intensity, timing, and number of recurrences of inter-loop ISI depend on the length of the loop and the half-life $T_{1/2}$ of GFPD. The intensity of inter-loop ISI can be reduced by using the EX.

3) Offset ISI: As GFPD molecules in the OFF state disperse in the system over multiple loops, the inter-loop ISI, characterized by distinct drops in fluorescence intensity, undergoes a gradual transformation to a temporal offset in the observed fluorescence intensity, which we refer to as offset ISI. The intensity of offset ISI depends on the irradiation intensity used at the TX, symbol duration T_I, and half-life $T_{1/2}$ of GFPD. The intensity of offset ISI can be reduced by using the EX.

4) Permanent ISI: After prolonged exposure to light, GFPD molecules may undergo an irreversible degradation as a consequence of photobleaching effects (cf. Section II-B4). While the decrease in fluorescence intensity resulting from offset ISI is reversible, photobleaching is not. Thus, photobleaching causes an irreversible reduction of the number of functional GFPD molecules available for modulation. Consequently, this leads to an overall decrease in the received fluorescence signal intensity over time. As a result, we observe a deterioration of the communication performance. Since GFPD molecules are irradiated by the EX, the RX, and the TX in the testbed, all three light sources contribute to photobleaching. Therefore, we refer to the fractions caused by the TX, EX, and RX as permanent ISI, EX bleaching, and measurement bleaching, respectively. Note that only photobleaching caused by the TX is interpreted as ISI, since it can be varied by varying the transmitted signal, whereas the photobleaching caused by EX and RX is independent of the transmitted sequence.

IV. COMMUNICATION SCHEME

This section introduces the proposed communication scheme, which includes modulation, synchronization, and detection.

A. Modulation and Reception

In Sections II-D1 and II-D3, we discussed modulation and reception qualitatively, respectively. This section provides a formal description of the transmission parameters, their effects on the MC signal, and the detection at the RX.

To transmit a symbol $i[k] \in \{0, 1, \ldots, M-1\}$, the TX is turned on with a corresponding light intensity I_i^{TX} for irradiation duration T_I. Here, k and $M = 2^{\eta}$ with $\eta \in \mathbb{N}$, where $\mathbb{N}$ is the set of positive integers, denote the symbol index and the modulation order, respectively. T_I is

followed by the guard interval of duration T_G, which results in $T_S = T_I + T_G$, cf. Section II-D1, and a data rate R of

$$R = \frac{\log_2 M}{T_S} . \tag{1}$$

During the irradiation process, the GFPD in the tube section of the TX undergoes a state transition (from ON to OFF) when hit by the emitted photons, reducing the local fluorescence. Increasing light intensity I^{TX} increases the hit probability, allowing control over the local fluorescence. This enables higher-order modulation with distinct fluorescence drops for different symbols i. In particular, in this work, we modulate the light intensity ratio ρ_i for symbol i as

$$\rho_i = \frac{I_i^{TX}}{I_{max}^{TX}} = \frac{3i}{4(M-1)} + \frac{1}{4}, \tag{2}$$

i.e., ρ_i is determined as the ratio of I_i^{TX} to the maximum available light intensity I_{max}^{TX}. Eq. (2) shows that ρ_i ranges from $1/4$ to 1, i.e., we do not assign intensity ratio zero to any symbol. This guarantees that the transmission of all symbols is distinct from the idle channel state, i.e., a turned off TX. This is necessary for symbol-by-symbol synchronization, as described in Section IV-B. On the RX side, the spectrometer periodically measures the local fluorescence by sampling with time interval Δt. After isolating the part of the signal close to the wavelength of interest, i.e., $\lambda_E = 529\,\text{nm}$, and normalizing[3] the maximum signal value to 1, the discrete-time received signal $r(t_n) \in [0,1]$ is obtained, where $t_n = n\Delta t$, with $n \in \mathbb{N}_0$. Here, $\mathbb{N}_0$ denotes the set of non-negative integers.

B. Synchronization

Synchronization is an integral part of any communication system and is required for demodulation. While in stationary environments it can be sufficient to synchronize once at the beginning of the transmission of a data packet, the task of synchronization becomes critical – and more challenging – when dealing with non-stationary communication channels. Sources of this non-stationarity can be, for example, closed-loop ISI effects, TX and RX movement, or a time-varying flow velocity. In this section, we propose synchronization schemes consisting of a transmission start detection and symbol-by-symbol synchronization. Hence, they address the aforementioned synchronization challenges.

1) Transmission Start Detection: Prior to the initiation of demodulation, the RX must detect that data transmission has started. To this end, a simple threshold-based trigger scheme is used, where transmission is assumed to have started when $r(t_n)$ drops below a threshold ξ_T. For this, $r(t_n)$, which prior the to first transmission contains only noise, is used to estimate the noise statistics. Then, ξ_T is determined based on the noise statistic. We assume that the noise arises from many small, independent sources of randomness, e.g.,

---

[3]The *ThorSpectra software* internally scales the received fluorescence intensity in a non-transparent manner. Comparing absolute fluorescence values from different experiments is therefore not possible. Instead, it is useful to compare relative values, i.e., trends of the measured fluorescence intensities, which is guaranteed by the proposed normalization.

thermal noise in the spectrometer, photon noise, i.e., the distribution of photons emitted by coherent light [43] from the RX LED, etc. Hence, applying the central limit theorem, we model the noise as Gaussian distributed.

Formally, before transmission has started, we collect a set of samples $\mathcal{K}[\tau] \triangleq \{r(t_n) | n \in \{\tau N_\mathrm{T}, \tau N_\mathrm{T} + 1, \ldots, (\tau+1)N_\mathrm{T} - 1\}\}$ of size N_T for $\tau \in \mathbb{N}_0$. Next, $\mathcal{K}[\tau]$ is used to fit a Normal distribution with mean $\hat{\mu}[\tau] = \frac{1}{N_\mathrm{T}} \sum_{r(t_n) \in \mathcal{K}[\tau]} r(t_n)$ and variance $\hat{\sigma}^2[\tau] = \frac{1}{N_\mathrm{T}-1} \sum_{r(t_n) \in \mathcal{K}[\tau]} (r(t_n) - \hat{\mu}[\tau])^2$ assuming independent and identically distributed samples, i.e., $r(t_n) \sim \mathcal{N}(\hat{\mu}[\tau], \hat{\sigma}^2[\tau])$. Finally, we obtain the threshold value $\xi_\mathrm{T}[\tau] = \Phi^{-1}(p_\mathrm{FA}; \hat{\mu}[\tau], \hat{\sigma}^2[\tau])$ for which a desired false alarm probability p_FA, i.e., the residual risk of an incorrect decision that transmission has started, is achieved. Here, $\Phi^{-1}(\cdot)$ denotes the inverse of the Gaussian cumulative distribution function.

The obtained $\xi_\mathrm{T}[\tau]$ is applied to the next sample set $\mathcal{K}[\tau+1]$. The transmission start is detected based on

$$t_\mathrm{TS} = \min_{\forall \tau}\{t_n | r(t_n) \leq \xi_\mathrm{T}[\tau],\ r(t_n) \in \mathcal{K}[\tau+1]\}, \tag{3}$$

where t_TS denotes the time at which transmission has started. Since $r(t_n)$ may decreases (slowly) over time due to photobleaching, this process is continuously repeated to ensure that ξ_T is periodically adjusted until a transmission start has been detected[4].

2) Symbol Synchronization: Synchronization guarantees a temporal alignment of the RX with the TX. For the testbed, we use a symbol-by-symbol synchronization approach [29], which correlates the processed received signal[5] $\tilde{r}(t_n)$ with a receive template filter $g(t_n)$ to obtain the synchronization metric

$$\Lambda(t_n) = \mathbf{g}^\top \tilde{\mathbf{r}}(t_n), \tag{4}$$

based on which the symbol start time $\hat{t}_\mathrm{s}[k]$ is estimated[6]. Here, $\mathbf{g} = \begin{bmatrix} g(t_0) & g(t_1) & \ldots & g(t_{\mathrm{N}-1}) \end{bmatrix}^\top$ and $\tilde{\mathbf{r}}(t_n) = \begin{bmatrix} \tilde{r}(t_n) & \tilde{r}(t_{n+1}) & \ldots & \tilde{r}(t_{n+\mathrm{N}-1}) \end{bmatrix}^\top$ are the vector representations of $g(t_n)$ and $\tilde{r}(t_n)$, respectively, where N is the filter length and $[\cdot]^\top$ denotes the transpose operator. Two synchronization schemes are employed: Correlation-based synchronization (CS) and differential correlation-based synchronization (DCS).

- *Correlation-based Synchronization (CS)*: The CS scheme utilizes the cross-correlation between the processed received signal $\tilde{r}(t_n) = 1 - r(t_n)$, which captures the deviation from maximum fluorescence, and a corresponding receive filter $g(t_n) \in \{g_\mathrm{C}^\mathrm{D}(t_n), g_\mathrm{C}^\mathrm{B}(t_n)\}$. Details of how the data-based receive filter $g_\mathrm{C}^\mathrm{D}(t_n)$, referred to as smoothed correlation filter (SCF), and the blind receive filter $g_\mathrm{C}^\mathrm{B}(t_n)$, referred to as blind correlation filter (BCF), are obtained, respectively, are provided in Section IV-C.

---

[4]Note that detecting the end of transmission is not needed, as we assume fixed-length messages.

[5]In particular, we use $\tilde{r}(t_n) \in \{1 - r(t_n), r(t_{n+1}) - r(t_n)\}$, as explained in detail in the next paragraph.

[6]Note that $\hat{t}_\mathrm{s}[k]$ does not correspond to the actual symbol start time, as the channel-related propagation delay is not known at the RX. Instead, it represents the RX's estimate of when a new symbol starts based on the selected template signal/filter.

- *Differential Correlation-based Synchronization (DCS)*: The DCS scheme is designed to mitigate the effects of slowly time-varying processes, such as offset-ISI, and utilizes the cross-correlation between the *differential* received signal $\tilde{r}(t_n) = r_D(t_n) = r(t_{n+1}) - r(t_n)$ and a corresponding *differential* receive filter $g(t_n) \in \{g_D^D(t_n), g_D^B(t_n)\}$. Note that in this case the corresponding vectors $\mathbf{g}$ and $\tilde{\mathbf{r}}(t_n)$ in (4) have dimension $N-1$, as the forward difference cannot be computed for the last vector entry. Details of how the data-based differential receive filter $g_D^D(t_n)$, referred to as smoothed differential correlation filter (SDCF), and the blind differential receive filter $g_D^B(t_n)$, referred to as blind differential correlation filter (BDCF), are obtained, respectively, are provided in Section IV-C.

a) Symbol-by-symbol synchronization: In the proposed symbol-by-symbol scheme, synchronization for the symbol in symbol interval k relies on the last estimated symbol start time $\hat{t}_s[k-1]$. A good initial guess for the start of the current symbol is given by $\tilde{t}_s[k] = \hat{t}_s[k-1] + T_S$. Note that $\tilde{t}_s[k]$ would also be the best estimate, if the previous estimate was accurate and the channel had not changed. Next, we define a search interval around $\tilde{t}_s[k]$ as $\mathcal{T}^{\text{search}}[k] \triangleq [\tilde{t}_s[k] - r\,T_S, \tilde{t}_s[k] + r\,T_S]$. Here, $r \in [0,1]$ denotes the normalized search radius, which can be adjusted based on the channel statistics, i.e., the stationarity of the channel. The start time $\hat{t}_s[k]$ of the current symbol interval k is obtained as

$$\hat{t}_s[k] = \underset{t_n \in \mathcal{T}^{\text{search}}[k]}{\arg\max} \, \Lambda(t_n). \tag{5}$$

This process is carried out for each symbol interval until the end of the transmission. The proposed synchronization method can adjust to fluctuations of the propagation delays in the channel within a single symbol interval as long as the true symbol start time is within the search interval.

b) Synchronization initialization: Since for the first symbol interval there is no previous estimate $\hat{t}_s[-1]$, we utilize the detected transmission start time as initial estimate, $\tilde{t}_s[0] = t_{TS}$, and set the search radius to $r = 0.5$ – resulting in search interval $\mathcal{T}^{\text{search}}[0] = [\tilde{t}_s[0] - \frac{T_S}{2}, \tilde{t}_s[0] + \frac{T_S}{2}]$. Even if t_{TS} does not correspond to a false alarm, it may still be a suboptimal estimate for the first symbol start. Therefore, choosing search radius $r = 0.5$ ensures that the best estimate for the first symbol start time is within the search interval. Synchronization then proceeds as described above.

C. Receive Filters

Two different approaches are used to obtain receive filters for the CS and the DCS schemes, namely a data-based approach and a blind filter approach. Although these filters are akin to a matched filter, we do no refer to them as such, as we cannot guarantee their optimality with respect to (w.r.t.) the achieved signal-to-noise ratio.

1) Data-Based Receive Filters: For each T_I considered in this work, a separate experiment was performed to obtain the typical shape of the received signal for that irradiation duration, on the basis of which the data-based filter was determined. Each of these experiments
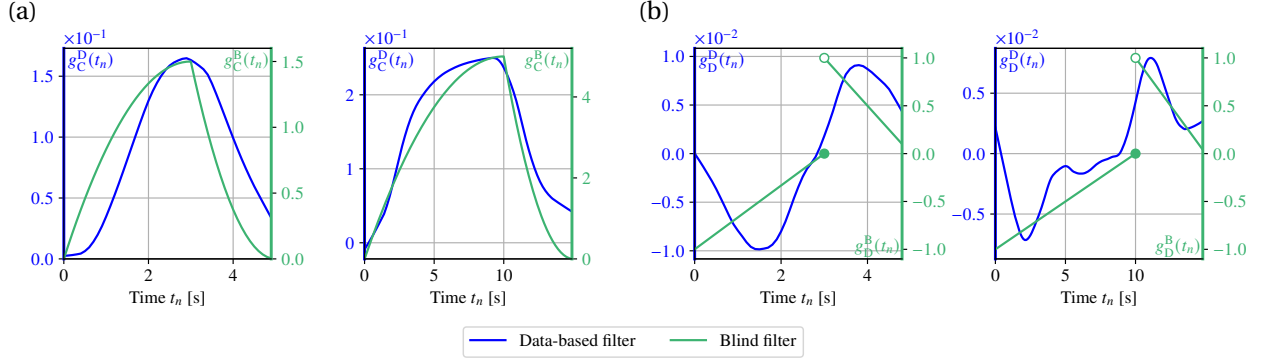
(a)
(b)

Data-based filter   Blind filter

Figure 2. Data-based receive filters and blind receive filters in comparison for two different configurations: $T_I = 3\,\text{s}$, $T_S = 5\,\text{s}$ (on the left) and $T_I = 10\,\text{s}$, $T_S = 15\,\text{s}$ (on the right) for the CS (a) and the DCS scheme (b), respectively.

consisted of a binary transmission of a single bit 1 repeated 11 times at 60 second intervals. The 11 individual received signals obtained in this way are referred to as signal responses (SRs) $s_r(t_n)$. To derive the data-based filter, the first SR is discarded and the remaining SRs are averaged and further smoothed using locally weighted polynomial regression [44] to obtain $\bar{s}_r(t_n)$. Ignoring the first SR is necessary because in the beginning almost all GFPDs are in the equilibrium state, cf. Section II-B, and therefore the fluorescence decay for the first SR is higher than for the following SRs. Then, the SCF, $g_C^D(t_n) = 1 - \bar{s}_r(t_n)$, $n \in \{0, 1, \ldots, N-1\}$, and the SDCF, $g_D^D(t_n) = \bar{s}_r(t_{n+1}) - \bar{s}_r(t_n)$, $n \in \{0, 1, \ldots, N-2\}$, are obtained by limiting them to an N and N−1 samples long signal, respectively, i.e., limiting them such that their lengths match the lengths of the corresponding $\tilde{\mathbf{r}}(t_n)$, cf. (4). The resulting receive filters $g_C^D(t_n)$ and $g_D^D(t_n)$ are shown in blue in Fig. 2a and Fig. 2b, respectively, exemplarily for two different symbol durations T_S. Fig. 2a shows that $g_C^D(t_n)$ increases over the irradiation durations $T_I = 3\,\text{s}$ (left subplot in Fig. 2a) and $T_I = 10\,\text{s}$ (right subplot in Fig. 2a), and decreases during the subsequent guard interval. For $T_S = 5\,\text{s}$ (left subplot in Fig. 2a), $g_C^D(t_n)$ is bell-shaped, while for the longer symbol duration, $T_S = 15\,\text{s}$ (right subplot in Fig. 2a), we see that $g_C^D(t_n)$ reaches a value of 0.25, before decreasing after $t_n = T_I = 10\,\text{s}$. In Fig. 2b, we see that the shape of $g_D^D(t_n)$ follows the derivative of $-g_C^D(t_n)$. Hence, it has a negative and a positive dip. For $T_S = 15\,\text{s}$ (right subplot in Fig. 2b), $g_D^D(t_n)$ shows some fluctuations around $t_n = 6\,\text{s}$, caused by noise that is amplified by the differentiation operation.

2) Blind Receive Filter: In cases where the data-based filter cannot be obtained in advance, we propose blind filters as surrogates for both the CS and DCS schemes, respectively. For these blind filters, we aim to capture roughly the shape of the data-based filters, with the goal of achieving a solution that is applicable across a broad range of unknown parameters without significant performance loss. For the sake of a simple and practical implementation, we limit the modeling of the blind filters to piecewise polynomials. Hence, the impulse responses of the proposed blind filters BCF, $g_C^B(t_n)$, and BDCF, $g_D^B(t_n)$, are given as follows,

$$g_C^B(t_n) = \begin{cases} -\frac{t_n^2}{2T_I} + t_n, & 0 \le t_n \le T_I \\ \frac{0.5\,T_I}{(T_S - T_I)^2}(t_n^2 - 2T_S t_n + T_S^2), & T_I < t_n \le T_S \\ 0, & \text{otherwise} \end{cases} \tag{6}$$

and

$$g_{\mathrm{D}}^{\mathrm{B}}(t_n) = \begin{cases} \frac{t_n}{T_{\mathrm{I}}} - 1, & 0 \leq t_n \leq T_{\mathrm{I}} \\ \frac{T_{\mathrm{S}} - t_n}{T_{\mathrm{S}} - T_{\mathrm{I}}}, & T_{\mathrm{I}} < t_n \leq T_{\mathrm{S}} \\ 0, & \text{otherwise} \end{cases}$$ (7)

respectively. $g_{\mathrm{C}}^{\mathrm{B}}(t_n)$ and $g_{\mathrm{D}}^{\mathrm{B}}(t_n)$ are plotted in green in Fig. 2a and Fig. 2b, respectively, exemplarily for two different symbol durations T_{S}. Fig. 2a shows that the shapes of the data-based filter $g_{\mathrm{C}}^{\mathrm{D}}(t_n)$ and the blind filter $g_{\mathrm{C}}^{\mathrm{B}}(t_n)$ are quite similar, while those of the differential filters $g_{\mathrm{D}}^{\mathrm{D}}(t_n)$ and $g_{\mathrm{D}}^{\mathrm{B}}(t_n)$ in Fig. 2b are more different. We will show in Section VI-C2 that despite these visible differences, the use of blind filters only leads to a small loss in performance compared to the use of data-based filters. In addition, blind filters do not require data collection, which justifies their use. Note that the blind filters are defined independent of each other as this leads to better results, i.e., $g_{\mathrm{D}}^{\mathrm{B}}(t_n)$ is not necessarily the sectional derivative of $g_{\mathrm{C}}^{\mathrm{B}}(t_n)$. Furthermore, note that the scaling of the data-based filters and the blind filters are different. However, for a given synchronization scheme, adjusting the scaling of any receive filter has no impact on the decisions derived from (4) and (5), since the operation in (4) is linear. Therefore, no scaling adjustment is needed.

D. Symbol Detection

For symbol detection, we use a single detection sample $d[k]$. Here, the detection sample is chosen to be the filtered received signal for the estimated symbol start time $\hat{t}_{\mathrm{s}}[k]$, which was determined by the proposed synchronization scheme, i.e.,

$$d[k] = \mathbf{g}^{\top} \tilde{\mathbf{r}}(\hat{t}_{\mathrm{s}}[k]).$$ (8)

In (8), correlation-based detection and differential correlation-based detection are employed, if CS and DCS was used for synchronization, respectively. Hence, when CS and DCS are mentioned in the following, this therefore also refers to the detection scheme used.

For detection, we employ an adaptive (multi-)threshold detector that periodically adjusts its thresholds based on previously detected symbols to account for the gradual reduction of the fluorescence over time due to photobleaching. Let $\Xi[l] \triangleq \{\xi_0, \xi_1, \ldots, \xi_{M-2}\}$ denote the set of detection thresholds, where ξ_j, $j \in \{0, 1, \ldots, M-2\}$, and l denote the individual threshold and the threshold set index, respectively. Additionally, we assume without loss of generality (w.l.o.g.) that $\Xi[l]$ is ordered in ascending order, i.e., $\xi_j < \xi_{j+1}$. For the employed single-sample detection, the transmitted symbol $\hat{i}[k]$ is determined as follows

$$\hat{i}[k] = \max\{j \mid j \in \{0, 1, \ldots, M-2\} \wedge d[k] \geq \xi_j\},$$ (9)

i.e., the symbol decision is based on $d[k]$ and $\Xi[l]$ only.

1) Detection Initialization: To determine the initial set of thresholds, $\Xi[0]$, each transmission starts with a random sequence of χ symbols. This sequence is used to allow the system

to settle[7] and is not considered for detection. Next, P pilot symbols are transmitted, where each $i \in \{0, 1, \ldots, M-1\}$ is sent at least once. The corresponding detection samples $d[k]$ form the initial sets $\mathcal{S}_i[l=0] \triangleq \{d[\mu] | \mu \in \{\chi, \chi+1, \ldots, \chi+P-1\} \wedge i[\mu] = i\}$, $i \in \{0, 1, \ldots, M-1\}$. The average of each set can be computed as follows

$$\bar{S}_i[l] = \frac{1}{|\mathcal{S}_i[l]|} \sum_{s \in \mathcal{S}_i[l]} s \, . \tag{10}$$

Here, $|\cdot|$ denotes the cardinality of a set. Hence, we use $l = 0$ in (10) to determine the averages $\bar{S}_i[l=0]$ of the initial sets $\mathcal{S}_i[l=0]$. Finally, the threshold values are computed as the means of the $\bar{S}_i[l]$ of adjacent sets:

$$\xi_j[l] = \frac{\bar{S}_{j+1}[l] + \bar{S}_j[l]}{2} \, , \tag{11}$$

for $j \in \{0, 1, \ldots, M-2\}$. Thus, to obtain the initial set of thresholds, $\Xi[0]$, we use $l = 0$ in (11).

2) Adaptation Algorithm: The duration for which the threshold set is valid has an upper limit that is determined by the coherence time of the channel. Therefore, a new set of thresholds must be determined after a certain number of detected symbols F. In contrast to the initial set of thresholds $\Xi[0]$, which is determined based on the P pilot symbols, the *update* of the set of thresholds requires only previously detected *data symbols*, i.e., no pilot symbols are used to update the threshold values. The corresponding update algorithm is described next.

For this, we relate the symbol index k to the currently valid threshold set index l via $l = \lfloor \frac{k-\chi-P}{F} \rfloor$, where $\lfloor \cdot \rfloor$ denotes the floor function. Note that l is not defined for $k < P + \chi$ because the first thresholds are computed only after the P pilot symbols have been received.

Similar to the initial sets $\mathcal{S}_i[l=0]$, we define sets

$$\mathcal{S}_i[l] \triangleq \{d[\mu] | \mu \in \{lF + \chi + P - W, \ldots, lF + \chi + P - 1\} \wedge \hat{i}[\mu] = i\} \, , \tag{12}$$

for $l > 0$ and $F + P - W \geq 0$. Here, W denotes the window width that determines the number of past samples $d[k]$ used for reevaluation. Finally, using (10) and (11), we obtain the new set of thresholds $\Xi[l]$.

In contrast to the pilot symbol sequence, now it is not guaranteed that all symbol values will be present in the W previously received symbols, i.e., some sets may remain empty $(|\mathcal{S}_i[l]| = 0)$. For this special case, the corresponding new thresholds cannot be determined directly using (10) and (11). We determine the differences between the new thresholds and the previous thresholds for the subset of thresholds for which this is possible, i.e., $\delta_q[l] = \xi_q[l] - \xi_q[l-1]$ for $q \in \mathcal{Q} \triangleq \{j | |\mathcal{S}_{j+1}[l]| \neq 0 \wedge |\mathcal{S}_j[l]| \neq 0\}$ with $j \in \{0, 1, \ldots, M-2\}$. The thresholds corresponding to the empty sets are subsequently obtained by adjusting the previous threshold value according to the *average* change across all thresholds $\Delta[l] =$

---

[7]The experiment is initially in a settling phase caused by the offset ISI, which develops slowly over successive transmissions and remains relatively constant after several symbols. Section VI-C1 presents experimental results that illustrate the transient phase of the testbed.

$\frac{1}{|\mathcal{Q}|} \sum_{q \in \mathcal{Q}} \delta_q[l]$ as $\xi_j[l] = \xi_j[l-1] + \Delta[l]$ for $j \notin \mathcal{Q}$. For the rare case, for which no new threshold can be determined, i.e., $|\mathcal{S}_j[l]| = 0 \vee |\mathcal{S}_{j+1}[l]| = 0, \forall j$, the thresholds retain their previous values, i.e., $\Xi[l] = \Xi[l-1]$.

V. PERFORMANCE METRICS

In this section, we describe the quantitative and qualitative communication-specific metrics employed to evaluate MC performance in the proposed testbed.

A. Bit Error Rate and Data Rate

We define an *empirical* BER for our system. The BER is a standard metric for quantifying the performance of any communication scheme. For the bit-to-symbol mapping, we use Gray mapping [45, p. 100] $G : \{0,1\}^{\log_2(M)N_{\text{Sym}}} \to \{0,\ldots,M-1\}^{N_{\text{Sym}}}$. Hence, the bit sequences corresponding to symbol sequences $\mathbf{i} \in \{0,1,\ldots,M-1\}^{N_{\text{Sym}}}$ and $\hat{\mathbf{i}} \in \{0,1,\ldots,M-1\}^{N_{\text{Sym}}}$, i.e., the transmitted and estimated symbol sequences, are obtained as $\mathbf{i}_G = G^{-1}(\mathbf{i})$ and $\hat{\mathbf{i}}_G = G^{-1}(\hat{\mathbf{i}})$, respectively. In our case, since the use of pilot symbols is required for calibration of all our detection techniques, the BER is obtained as

$$\text{BER} = \frac{\sum_{b=\log_2(M)P}^{\log_2(M)N_{\text{Sym}}-1} \left| \mathbf{i}_G[b] - \hat{\mathbf{i}}_G[b] \right|}{(N_{\text{Sym}} - P)\log_2(M)} . \tag{13}$$

Note that this equals the Hamming distance between $\mathbf{i}_G$ and $\hat{\mathbf{i}}_G$ normalized to the bit sequence length excluding the sequence part corresponding to the pilot symbols P. Thus, the empirically defined BER is the number of erroneously demodulated bits scaled by the number of all transmitted bits.

B. Absolute Mean Euclidean Distance

In some cases the BER is not insightful, e.g., if the transmission sequence length is too short for an accurate estimation of the BER or if the MC system is in the low BER regime, where irrespectively of the chosen settings, for the evaluated transmission sequence length, BER $= 0$ is obtained. For such cases, we introduce the AMED metric as follows

$$\text{AMED} = \min_{i' \neq i''} |\bar{S}_{i'}[l] - \bar{S}_{i''}[l]| ; \qquad \forall i', i'' \in \{0,1,\ldots,M-1\} , \tag{14}$$

where we employ (10) and (12).

As can be seen from (14), the AMED is the minimum Euclidean distance between the means of the samples $d[k]$ received over W symbol intervals. Consequently, the AMED reflects the extent to which the received samples of the various symbols differ. Compared to the BER, the AMED provides reliable values even for small numbers of samples, i.e., small W, and can therefore serve as an initial indicator of performance for cases where a BER evaluation is not meaningful or not possible.
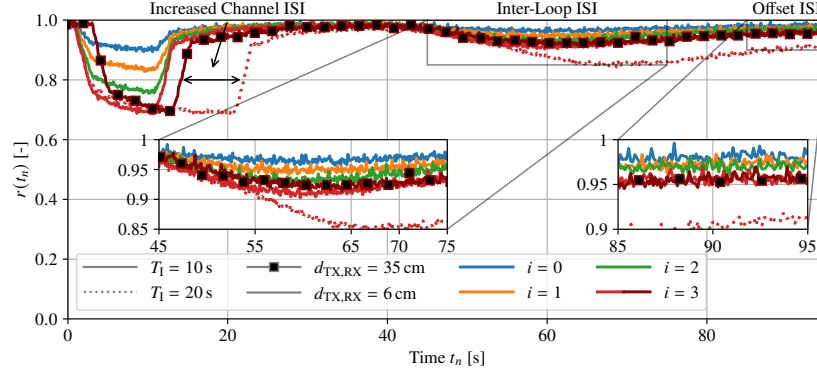
Figure 3. $r(t_n)$ of single symbol transmissions with $i \in \{0,1,2,3\}$ for different irradiation durations $T_I = 10\,\text{s}$ and $T_I = 20\,\text{s}$, and TX-RX distances $d_{TX,RX} = 6\,\text{cm}$ and $d_{TX,RX} = 35\,\text{cm}$. Three forms of ISI are visualized: channel ISI, inter-loop ISI, and offset ISI.

C. Eye Diagram

Eye diagrams are a well-established qualitative method to evaluate a communication system's performance [45, p. 603]. The use of eye diagrams to evaluate MC systems has been introduced in [20]. Plotting the received signal modulo the symbol duration generates the eye pattern. Effects such as ISI, various system parameters, including the use of a guard interval, and the effects of varying the modulation order affect the eye pattern and the eye opening, which can provide insights for system design and performance.

VI. EXPERIMENTAL RESULTS AND COMMUNICATION PERFORMANCE EVALUATION

In this section, we evaluate our testbed based on the previously proposed metrics and determine the impact of different system parameters. To obtain these results, in total more than 250 kbit of data were transmitted via MC in the testbed.

A. Illustration of the Different Types of ISI

The following experiments were conducted to illustrate three different types of ISI that occur in our testbed. The results are summarized in Fig. 3. In particular, individual symbols $i \in \{0,1,2,3\}$, indicated by different colors, are sent. Furthermore, for $i = 3$, we show results for two illumination durations, $T_I = 10\,\text{s}$ (solid line) and $T_I = 20\,\text{s}$ (dotted line), and two different transmission distances, $d_{TX,RX} = 6\,\text{cm}$ (no marker) and $d_{TX,RX} = 35\,\text{cm}$ (rectangular markers). Fig. 3 shows the corresponding received signals $r(t_n)$. In these experiments, the EX was turned off to increase the visibility of the ISI effects.

For $T_I = 10\,\text{s}$, Fig. 3 shows two drops in $r(t_n)$. The first drop around 10 s corresponds to the desired pulse sent by the TX, after which the signal returns back to its original level at around 30 s. The second drop, visible around 60 s, corresponds to inter-loop ISI, while the offset ISI is visible in the inset at 90 s. Both the inter-loop ISI and the offset ISI increase with increasing i. Since permanent ISI caused by photobleaching occurs after many transmission cycles only, it is not visible in Fig. 3. We observe from Fig. 3 that $r(t_n)$ returns back close to its initial value $r(t_n) = 1.0$ at a later time when the irradiation time is increased from $T_I = 10\,\text{s}$ (solid lines) to $T_I = 20\,\text{s}$ (dotted line), consequently increasing the channel ISI. Furthermore,

we observe that the depth of the fluorescence intensity drop of the first pulse remains the same, while the inter-loop ISI intensity increases significantly. From this, we infer that both the irradiation time T_I and which symbol i is transmitted have an influence on the inter-loop ISI. Moreover, Fig. 3 shows that the irradiation time T_I and which symbol i is transmitted also have an impact on the offset ISI. These observations suggest that there exists an optimal irradiation duration T_I. In particular, there exists a trade-off as T_I should be chosen large enough to produce a detectable signal, but small enough to prevent the undesired accumulation of ISI, as all forms of ISI increase when T_I is increased.

Finally, we observe from Fig. 3 that increasing the transmission distance from $d_{TX,RX} = 6\,cm$ (no marker) to $d_{TX,RX} = 35\,cm$ (rectangular markers) results in a later arrival of the first pulse at the RX, which is expected as the signal molecules have to propagate a longer distance. Furthermore, we observe that the pulse shape remains the same. Hence, we conclude that even a transmission distance of $d_{TX,RX} = 35\,cm$ is too small for diffusion to have an impact.

B. Transmission and Error-Free Detection of 90 kbit

In this section, we evaluate the performance of the testbed for long-term transmissions. The results are provided in Fig. 4. To this end, two experiments, one with EX and one without EX, were conducted over a period of 125 hours each, during which, in each case, $N_{Bit} = 90,000$ were transmitted using binary modulation at a data rate of $12\,bit\,min^{-1}$. The 90,000 bit were generated using a random 2000 bit sequence, which was repeatedly transmitted 45 times. These experiments aim to demonstrate the key advantage of the proposed waste-free, self-contained, and closed-loop testbed, namely enabling the long-term study of tube-based MC systems. During each experiment, the testbed was not subjected to any alterations. Specifically, neither new GFPD molecules were introduced nor were any substances extracted from the testbed. Instead, the same 9 mL of GFPD solution was employed throughout each experiment.

1) Received Fluorescence Signal: Fig. 4a shows the received signal $r(t_n)$ over time for both experiments with (blue curve) and without (orange curve) EX. The inset plots show the signals at three particularly interesting time instants: the beginning (left), the time of an (undesired and unexpected) fluorescence jump in one of the received signals (center), and the end of the transmission (right), alongside with the corresponding TX signal (green). Here, gray shaded areas in the inset plots indicate bit "1" transmissions. The inset plots of Fig. 4a show that, as expected, $r(t_n)$ exhibits large drops in fluorescence intensity for bit 1 transmissions and small drops in fluorescence intensity for bit 0 transmissions. This indicates that reliable communication is possible. We further observe from Fig. 4a that the general fluorescence level of the system decreases over time. This is due to offset ISI and photobleaching effects, i.e., the prevalence of temporarily and permanently off-switched GFPDs, respectively. We observe that, as expected, in the beginning ($t < 60,000\,s$), the average fluorescence level with EX is higher than without EX. However, later, the fluorescence for
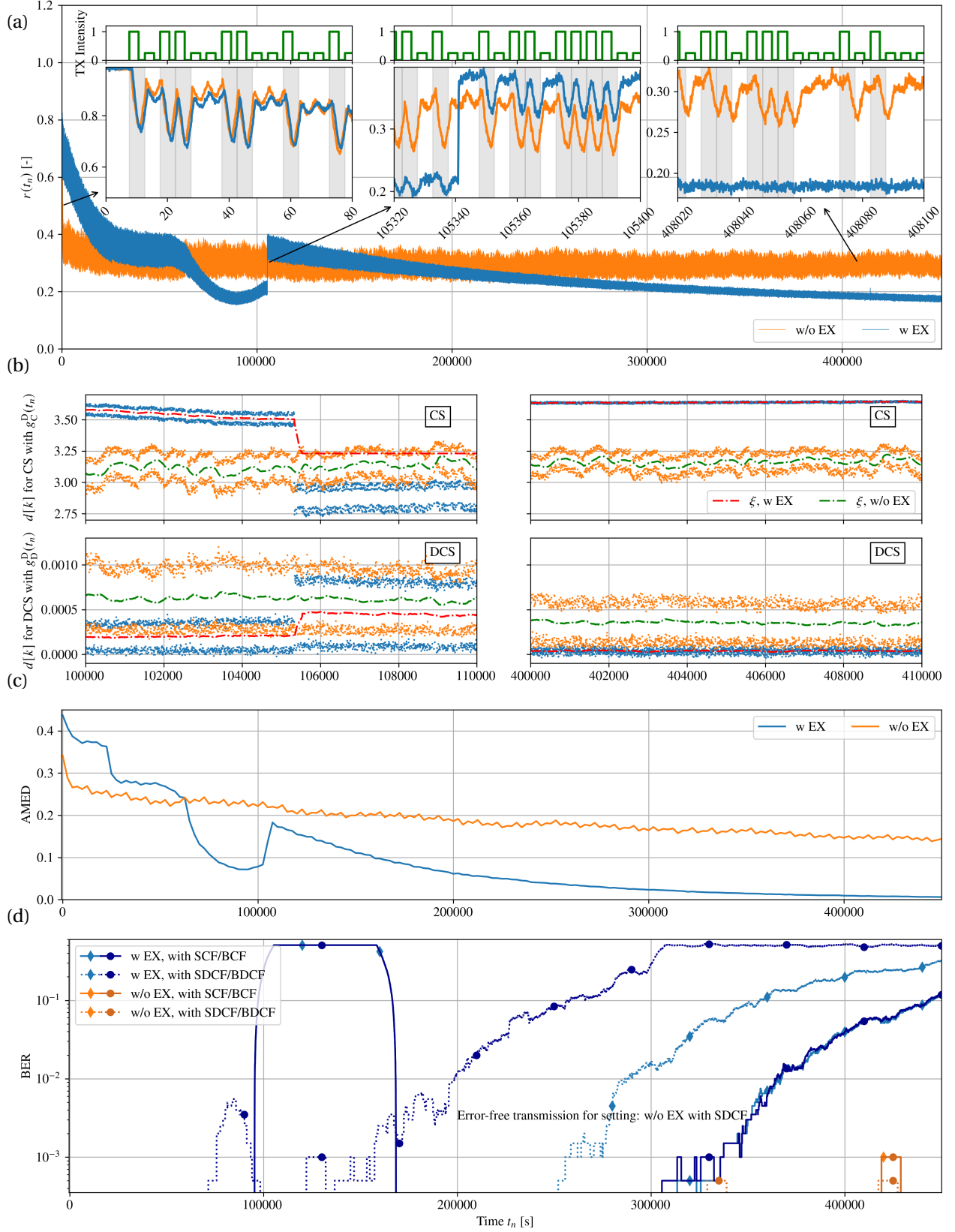
Figure 4. Evaluation of a long-term binary transmission with $T_S = 5$ s, $N_{Bit} = 90{,}000$, $p_{FA} = 10 \times 10^{-10}$, $\Delta t = 0.1$ s, $N = \lfloor \frac{T_S}{\Delta t} \rfloor$, $N_T = 50$, $r = 0.04$, $W = 50$, $F = 1$, $\chi = 80$, and $P = 130$ with (blue curves) and without (orange curves) EX. (a) Received signal over time. Shaded areas in the insets correspond to bit 1 transmissions. (b) Detection samples for different detection schemes using data-based receive filters and the corresponding thresholds around 27 h after starting data transmission (left panel) and at the end of transmission (right panel). (c) AMED between bit 1 and bit 0 transmissions over time. (d) Moving average BER (computed over the most recent 2000 bit) for the different detection schemes.

the case with EX clearly drops below that without EX. This indicates that the EX successfully mitigates offset ISI, which is the predominant immediate cause of a fluorescence decrease. At the same time, the EX enhances photobleaching as its use increases the number of photons that hit the GFPD molecules. The signal depicted in blue in the right inset plot reveals the increased photobleaching with EX, which results in a performance degradation. In particular, in this case, the number of GFPD molecules in the ON state that are available for off-switching at the TX is very low. The modulation at the TX thus exhibits fluorescence drops that cannot be discerned from measurement noise. This is not the case for the scenario without EX.

One peculiar feature of the considered experiment is the rapid fluorescence decrease ($t \approx 60{,}000\,\mathrm{s}$) and subsequent jump ($t \approx 110{,}000\,\mathrm{s}$) for the scenario with EX. While it is difficult to prove, we believe that this behavior is caused by an agglomeration of degraded GFPD molecules in the flow cell, i.e., the RX. Since degradation is caused by photobleaching, we expect this agglomeration will be more likely to occur in scenarios with EX than without EX. An agglomeration can significantly alter the measured fluorescence signal, as it acts as an undesirable physical light filter. This hypothesis matches the observed behavior, as a spontaneous detachment of the agglomeration would explain the re-establishment of the previous fluorescence level at $t \approx 110{,}000\,\mathrm{s}$.

2) Detection Samples: Fig. 4b shows the detection samples, cf. (8), obtained using the CS (top panels) and DCS schemes (bottom panels) alongside the respective adaptive thresholds. We focus on two particularly interesting time intervals: The left panels focus on the time around the fluorescence jump, while the right panels show the samples at the end of the transmission. Orange and blue dots correspond to the detection samples, cf. (8), for the setting without and with EX, respectively. Comparing the top and bottom panels, we observe that the threshold for the DCS scheme (bottom) quickly adapts to the fluorescence jump, while errors are caused for the CS scheme. The fluorescence jump, which predominantly results in an offset of the fluorescence, exerts a lower impact on the differential signal. Moreover, Fig. 4b confirms our prior observation that the experiment without EX exhibits a more stable long-term behavior. For instance, we observe from the right-hand panels in Fig. 4b that the bit 1 and bit 0 samples are still clearly separated by the threshold in the scenario without EX even after 400,000 s ($\approx$ 111h) of continuous transmission, while for the scenario with EX, the samples cannot be separated by either detection scheme. Interestingly, the advantage of the DCS scheme vanishes at the end of the transmission for the experiment with EX. The reason for this behavior is that the signal at this point is similar in magnitude to the noise. As the differentiation operation amplifies the noise, it starts to dominate the signal, which degrades the communication performance.

3) AMED Analysis: Fig. 4c shows the AMED, cf. (14), for the scenarios with and without EX over time. The metric is computed continuously over windows of $W = 500$ bit. As expected,

the AMED generally decreases over time, regardless of whether the EX is used or not. Initially, when the offset ISI is the dominant impairment, the use of the EX leads to a higher AMED. However, as photobleaching caused by the EX becomes pronounced, the AMED drops below that of the scenario without EX. In addition, the effect of the fast fluorescence decrease and subsequent jump is clearly visible in Fig. 4c. This is consistent with our previous observations for the fluorescence signal and the detection samples. Based on the AMED, the benefits of the EX for short transmissions become apparent, but they disappear for long sequences.

4) BER Analysis: Finally, Fig. 4d shows the empirical moving average BER, i.e., the BER calculated sequentially over the most recent 2000 symbols using (13), as a function of time for the different considered receive filters and the setting with and without EX, respectively. Plotting the BER this way enables us to analyze the causes of detection errors and whether the detectors allow for an adaptation to avoid subsequent errors or not. In Fig. 4d, the solid and dotted lines correspond to the use of the CS and DCS schemes, respectively, while the color indicates whether or not the EX was active. The diamond-shaped and round markers specify whether data-based or blind filters were used. We observe that, while the EX is in principle beneficial for short transmission times, for long transmission times, the BER is larger for the case with EX. This is, on the one hand, caused by the abnormal fast fluorescence decrease and fluorescence jump, and on the other hand, by the more severe photobleaching and the resulting low fluorescence level leading to a low signal-to-noise ratio. The former manifests itself in the sudden jump in the BER to 0.5 for the CS scheme around the occurrence of the fluorescence jump. Detection errors end when the fluorescence is back roughly to the level at which it was before the jump, such that the threshold becomes valid again. The decreasing signal-to-noise ratio manifests itself in a gradual increase of the BER over time. Here, the BER rises first for the DCS scheme, which can be attributed to the noise enhancement caused by differentiation. In contrast, without EX, transmission remains error-free for more than 300,000 s for both considered detection schemes. In fact, error-free transmission of around $N_{\mathrm{Bit}} = 90,000$ bit[8] is possible with the DCS scheme and the data-based receive filter $g_{\mathrm{D}}^{\mathrm{D}}(t_n)$.

C. BER vs. Data Rate: 8-ary Modulation with an Achievable Rate of 36 bit min^{-1}

We evaluate our testbed in terms of the achievable BER for various different data rates. Specifically, we experimentally determined the BER for 18 individual experiments, in each of which 2000 symbols (corresponding to 2000, 4000, or 6000 bit, depending on the modulation order) were transmitted. For each single experiment, a fresh GFPD sample was used in order to prevent dependencies between the experiments. For all results shown in this section, the EX was used. As we use $\chi = 80$ and $P = 130$, the BER values were determined based on 1,790 symbols.

---

[8]To be precise, with $\chi = 80$ and $P = 130$, $N_{\mathrm{Bit}} = 89790$ bit were detected error-free.
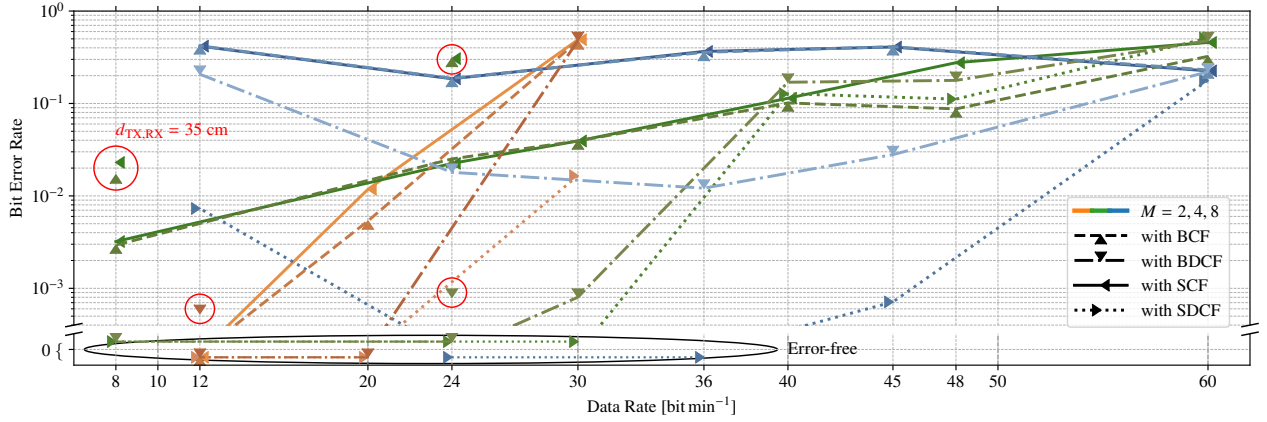
Figure 5. BERs for 18 individual experiments. Here, $p_{FA} = 10 \times 10^{-8}$, $\Delta t = 0.1\,\text{s}$, $N = \lfloor \frac{T_S}{\Delta t} \rfloor$, $N_T = 50$, $W = 50$, $F = 1$, $\chi = 80$, $P = 130$, and different search radius lengths $r \in [0.03, 0.12]$ are used. The red circles mark results obtained for $d_{TX,RX} = 35\,\text{cm}$.

Fig. 5 shows the achieved BERs for data rates between $8\,\text{bit}\,\text{min}^{-1}$ and $60\,\text{bit}\,\text{min}^{-1}$. In particular, modulation orders $M = 2$ (yellow), $M = 4$ (green), and $M = 8$ (blue), and symbol durations between $T_S = 2\,\text{s}$ and $T_S = 15\,\text{s}$ are used. The individual experiments thus correspond to transmission durations between $67\,\text{min}$ and $500\,\text{min}$. Furthermore, we present results for a transmission channel length of $d_{TX,RX} = 35\,\text{cm}$ (marked by red circles) to provide insight into the effect of the channel length and to prove that reliable communication is still feasible for longer channels. Experiments for which no errors were observed are displayed at the bottom of Fig. 5 after the axis break.

1) Effect of Modulation Order: Fig. 5 shows that, for all considered modulation orders examined, error-free transmission was experimentally achieved within a certain data rate region (for $M = 2$ from $12\,\text{bit}\,\text{min}^{-1}$ up to $20\,\text{bit}\,\text{min}^{-1}$, for $M = 4$ from $8\,\text{bit}\,\text{min}^{-1}$ up to $30\,\text{bit}\,\text{min}^{-1}$, and for $M = 8$ from $24\,\text{bit}\,\text{min}^{-1}$ up to $36\,\text{bit}\,\text{min}^{-1}$). For $M = 2$ and $M = 4$, we observe that the BER, as expected, increases with increasing data rate. For $M = 8$, when comparing the BERs for $24\,\text{bit}\,\text{min}^{-1}$ and $12\,\text{bit}\,\text{min}^{-1}$, we see that the BER is larger at $12\,\text{bit}\,\text{min}^{-1}$, which is not intuitive. However, when analyzing the received signal for this setting[9], we observed a gradual decrease in fluorescence intensity, similar to that described in Section VI-B1. We attribute this to the severe photobleaching when using $T_S = 15\,\text{s}$ with irradiation duration $T_I = 10\,\text{s}$. Therefore, the resulting weak received signal does not support error-free transmission for 8-ary modulation for this data rate.

Note that, for a given modulation order M, we increase the data rate by reducing the symbol duration T_S. However, T_S cannot be reduced arbitrarily, as this leads to an increase in channel ISI, which in turn results in an increased BER. Specifically, Fig. 5 reveals that only $M = 8$ can achieve error-free transmission at rates greater than $30\,\text{bit}\,\text{min}^{-1}$. Hence, for error-free transmission at high data rates, an increase in modulation order is necessary. For such a setting, where $M = 8$ and $T_S = 5\,\text{s}$ are used, details are provided next.

Fig. 6 shows the detection samples $d[k]$ for the DCS scheme using SDCF as receive filter.

---

[9]Unfortunately, the mentioned received signal cannot be shown in this paper due to space constraints. However, of course, the data for this received signal is included in the dataset that we have made publicly available on Zenodo, cf. Section VII-B.
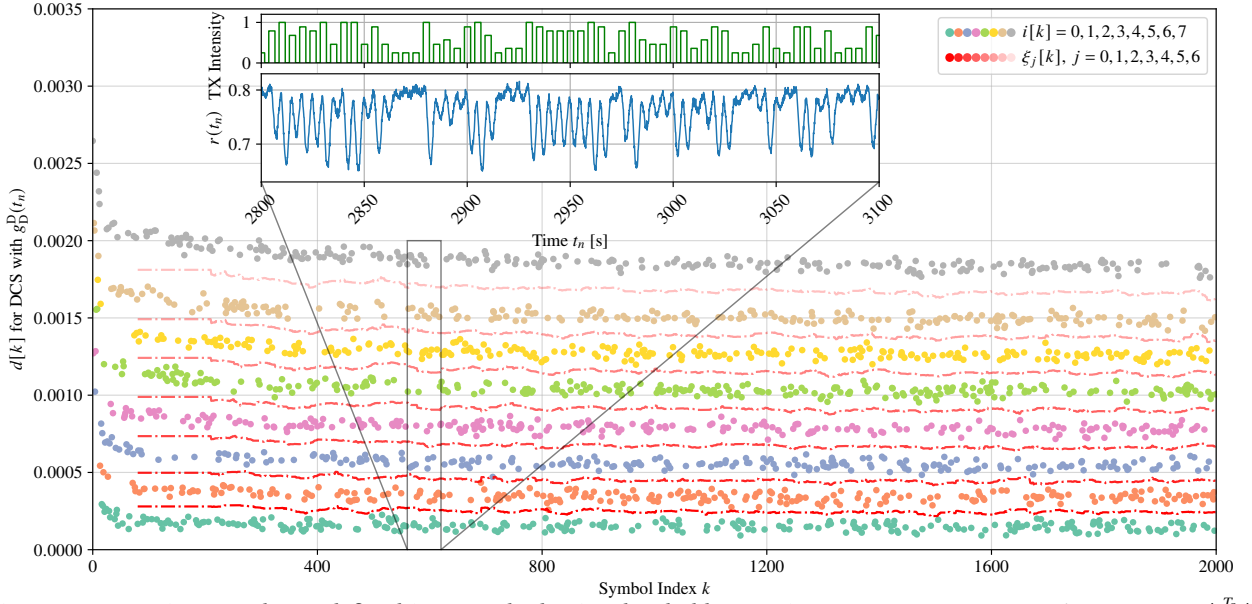
Figure 6. Detection samples as defined in (8) and adaptive thresholds over time. Here, $M = 8$, $T_S = 5\,\text{s}$, $\Delta t = 0.1\,\text{s}$, $N = \lfloor \frac{T_S}{\Delta t} \rfloor$, $N_T = 50$, $W = 50$, $F = 1$, $\chi = 80$, $P = 130$, and $r = 0.08$ are used. The detection samples are color-coded based on the corresponding transmit symbol $i[k] \in \{0, \ldots, M-1\}$. Inset plot: Corresponding received signal and TX intensity.

In Fig. 6, the different colors indicate the transmitted symbols $i[k] \in \{0, \ldots, M-1\}$, while the dash-dotted lines in the red monochrome color palette correspond to the adaptive thresholds $M-1$ used for symbol detection. Additionally, the inset in Fig. 6 shows the TX intensity and the received signal for the symbols transmitted in the interval $t \in [2800, 3100]\,\text{s}$.

From the inset in Fig. 6, we observe that the TX intensity is reflected in visible changes of the received signal, which shows distinct peaks. We further observe from Fig. 6 that, even for 8-ary modulation, the samples for the DCS scheme are well distinguishable w.r.t. the adaptive threshold values. Moreover, Fig. 6 shows that the experiment is in a transient phase at the beginning, which leads to a high variance of the sample values. The transient phase is caused by offset ISI, which develops slowly over successive transmissions and remains relatively constant after about 50 to 100 symbols. Therefore, the omission of the first $\chi = 80$ symbols is crucial to ensure that the thresholds ξ_j can be adequately initialized afterwards.

2) Effect of Receive Filter and Detection Method: In Fig. 5, we can also compare the BERs for the four filters proposed for detection: SCF (solid, leftwards pointing marker), BCF (dashed, upwards pointing marker), SDCF (dotted, rightwards pointing marker), and BDCF (dash-dotted, downwards pointing marker). Detection based on the differential signal, i.e., SDCF and BDCF, in many cases leads to a significantly lower BER in direct comparison to SCF and BCF. Furthermore, Fig. 5 shows that, as expected, the data-based filters (SCF and SDCF) are superior to the blind filters (BCF and BDCF), as evidenced by the lower BER.

We conclude that the DCS scheme is well suited for detection of higher-order modulation when used in combination with EX. However, the DCS scheme can be disadvantageous in long experiments, where the signal eventually becomes weak due to photobleaching, because of the noise enhancement introduced by the differentiation operation. In this case,
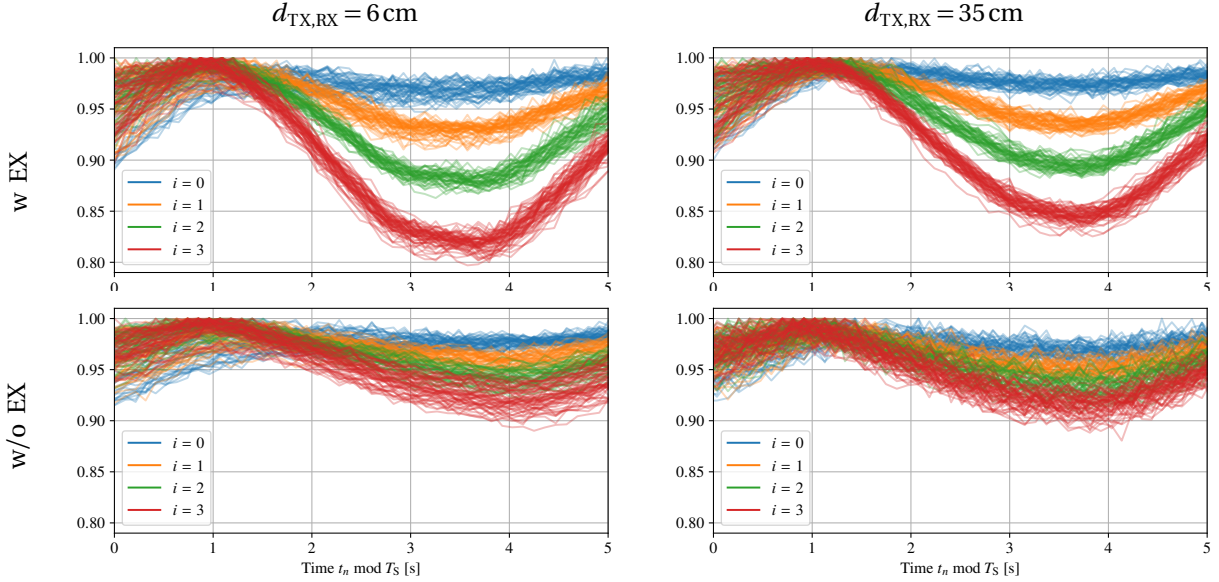
Figure 7. Eye diagrams. Here, $M = 4$, $T_S = 5\,\text{s}$, $T_I = 3\,\text{s}$, and $\Delta t = 0.1\,\text{s}$ are used.

the CS scheme is preferable, cf. Section VI-B.

3) Effect of Transmission Distance: Finally, Fig. 5 shows the effects of the elongation of the channel from $d_{\text{TX,RX}} = 6\,\text{cm}$ to $d_{\text{TX,RX}} = 35\,\text{cm}$. Three distinct settings have been analyzed: $M = 4$ with data rate $8\,\text{bit}\,\text{min}^{-1}$, $M = 2$ with data rate $12\,\text{bit}\,\text{min}^{-1}$, and $M = 4$ with data rate $24\,\text{bit}\,\text{min}^{-1}$. For these settings, error-free transmission is still possible even for $d_{\text{TX,RX}} = 35\,\text{cm}$ when using the SDCF as receive filter[10]. Moreover, we observe from Fig. 5 that for the detection schemes, where detection errors occur, the corresponding errors are larger for distance $d_{\text{TX,RX}} = 35\,\text{cm}$ compared to $d_{\text{TX,RX}} = 6\,\text{cm}$, which was expected. For example, for $M = 4$ and the CS scheme, the BER increases by one order of magnitude.

D. EX-Based ISI Mitigation in Short-Term Transmissions

In this section, we show that the EX is capable of ISI mitigation in short-term transmission. Fig. 7 shows eye diagrams for $M = 4$ and different experimental settings, including varying channel lengths and EX settings. The curves correspond to symbols $i[k]$ for $k \in \{100, 101, \ldots, 299\}$ out of a $N_{\text{Sym}} = 2000$ symbol long sequence being transmitted. Synchronization was achieved using the CS scheme with SCF as receive filter for all scenarios. We horizontally shifted the received signal $r(t_n)$ for each transmit symbol to have its maximum at 1 for better visibility. In Fig. 7, different transmit symbols i are denoted by different colors.

When the EX is used (top panels in Fig. 7), we observe three eyes, indicating that the different transmit symbols can be distinguished easily. This is especially evident for the short channel length of $d_{\text{TX,RX}} = 6\,\text{cm}$ (top left panel). Elongating $d_{\text{TX,RX}}$ results in a slightly smaller eye opening. Thus, the larger $d_{\text{TX,RX}}$ has only a small effect, which shows that, as analyzed theoretically in Section III-A, diffusion affecting the TX-RX link can be neglected for the $d_{\text{TX,RX}}$ considered in this work.

---

[10]Note that only the markers for BER > 0 are shown with the red circle. Error-free results for a distance of 35 cm are not indicated by a marker to avoid overloading the figure around BER $= 0$.

Table I

OVERVIEW OF SELECTED FLUID-BASED MC TESTBEDS

Signaling Molecule (Biocompatibility)	Data rate (bit/s)	BER (# transmitted bits)	Detection Method	Reference
Green Fluorescent Protein Dreiklang (GFPD) (✓)	0.6	0 (5370)	Differential Signal + Adaptive Threshold	This paper
Superparamagnetic Iron Oxide Nanoparticles (SPIONs) (✓)	10	0.0843 (600)	Convolutional Neural Network	[15]
Sodium chloride (NaCl) (✓)	5	0.002 (100 x 100)	μ Link Decoder with Channel Estimation and Sequence Detection	[17]
Colored Ink (✗)	1.5	1/312 (312)	Threshold	[18]
Acid/Base (✗)	2.63	0 (1080)	Recurrent Neural Network	[20]
Sodium Hydroxide (NaOH) (✗)	1/375	0.04 (100)	Threshold	[21]
Hydrogen Chloride (HCl) (✗)	1/27	0.022 (1000)	Adaptive Threshold	[32]
Transfer DNA (tDNA) (✓)	1/120	0 (20)	Differential Signal + Threshold	[33]
Glucose ($C_6H_{12}O_6$) (✓)	2	0.05 (654)	Machine Learning	[46]

If the EX is turned off, we see that the eyes are closed (bottom panels in Fig. 7), i.e., the received signals for the different transmit symbols i are largely overlapping. In particular, we observe that the received signals for the same symbol i vary more without EX compared to when the EX is used, which we attribute to larger inter-loop and offset ISI. We observe from Fig. 7 that for the considered settings, reliable communication using 4-ary modulation without EX can be difficult and may require sophisticated equalization techniques at the RX.

In summary, employing an EX has some benefits (ISI-mitigation, cf. Section VI-D), but also undesired side-effects (photobleaching of GFPD, cf. Section VI-B). Based on our results, we conclude that the use of an EX is advisable for short-term transmission, high modulation orders, and short symbol durations T_S.

VII. TESTBED COMPARISON AND DATA SHARING

In this section, we compare our testbed to other fluid-based testbeds, and provide information regarding the sharing of our data and code.

A. Comparison with Other Testbeds

Our comparison is focused on the experimentally determined BERs, the detection schemes used, and the efficiency of data transmission. Table I provides a selected overview of fluid-based MC testbeds, listing for each testbed the signaling molecule used, the lowest reported BER, the data rate achieving this BER, the length of the bit sequence transmitted, and the employed detection method.

Providing a fair and still meaningful comparison between existing MC testbeds and the proposed testbed is challenging due to some fundamental differences. In particular, none of the existing works has considered a closed-loop and self-contained topology. As a result, only our testbed is confronted with the challenge of resolving inter-loop ISI, offset ISI, and permanent ISI. In addition, all other testbeds require and use a much larger number of signaling molecules due to their open topology. The resulting low molecule efficiency, which in [47] has been defined as the number of bit transmitted per volume of dissolved signaling molecule solution, is a significant challenge in existing testbeds. The issue of low efficiency has been recognized and discussed [15], [16], [46]: In [15], an efficiency of $160 \, \mathrm{bit\,mL^{-1}}$ was achieved, which is still low compared to our testbed with $90,000/9 \, \mathrm{bit\,mL^{-1}} = 10,000 \, \mathrm{bit\,mL^{-1}}$;

in [46], the authors reported that some measurements had to be discarded because the TX ran out of molecules earlier than expected; and in [16], high costs were associated with the use of the testbed, resulting in a maximum evaluated bit sequence length of 8 bit[11].

Despite the different topologies and the challenges our testbed has to overcome, we achieve a data rate that is only an order of magnitude lower than the largest data rates reported in the MC literature, which are from [15][12]. At the same time, our testbed provides very reliable communication, i.e., very low BERs, while employing a low-complexity detection scheme that involves only differentiation of the received signal and an adaptive threshold detector. Quantifying the computational complexity of the detection schemes listed here is beyond the scope of this paper. However, methods based on machine learning, such as Convolutional Neural Networks [15] and Recurrent Neural Networks [20], as well as methods that explicitly take into account the memory effects caused by ISI [17], even if efficiently implemented using the Viterbi algorithm, are believed to have comparatively higher computational complexities.

B. Data Handling and Code Sharing

To promote transparency and enable experimental evaluation of new communication algorithms developed by the MC community, we publish our experimental data and the Python code for synchronization and detection in Zenodo and a Git repository under the CC BY and the MIT licenses, respectively. When used, the data and/or code can and should be cited using the corresponding Zenodo digital object identifier (DOI) [34]. The link to the Git repository can be found on Zenodo.

VIII. CONCLUSION

In this paper, we presented the first self-contained, closed-loop experimental MC system using media modulation. As the testbed leverages the reusable and biocompatible signaling molecule GFPD, long-term experiments without the need for repeated injection or removal of molecules were possible.

We developed a communication scheme which features higher order modulation, a noise-based wake-up method, blind and data-based synchronization, and adaptive threshold detection. Utilizing key performance metrics, such as AMED and BER, the quality and reliability of the testbed were demonstrated. Notably, we achieved error-free transmission of 5790 bit at $36\,\mathrm{bit\,min^{-1}}$. Moreover, we conducted the longest MC experiment to date, both w.r.t. the number of bits transmitted as well as the duration of the transmission. In particular, 90,000 bit were transmitted error-free over a period exceeding 5 days (125 h) at a data rate of

---

[11]The authors in [16] also reported that for such a short sequence a meaningful estimation of the BER was not possible. We believe that this is an example where the discussed alternative performance metrics, such as AMED and eye diagrams, are particularly useful.

[12]For the sake of completeness, we note that, to the best of our knowledge, the highest *achievable* data rate was reported in [48].

$12\,\text{bit}\,\text{min}^{-1}$, thereby setting a novel benchmark for long-term MC experiments. In total, only $9\,\text{mL}$ of GFPD solution were required for this long experiment, which serves to illustrate the efficacy of the media modulation approach. In order to encourage further research, we have made the experimental data (> 250 kbits) and the corresponding evaluation code available via open access on Zenodo and Github, respectively. This enables researchers to explore advanced methods (e.g., based on machine learning) for improving synchronization and detection performance, which are interesting future research directions. Moreover, the testbed can easily be expanded due to its modular and flexible design. For example, the incorporation of a branched tube network, which could emulate real biological environments, is of high practical interest.

REFERENCES

[1] L. Brand *et al.*, "Closed loop molecular communication testbed: Setup, interference analysis, and experimental results," in *Proc. IEEE Int. Conf. Commun.*, Jun. 2024, pp. 4805–4811.

[2] T. Nakano, A. W. Eckford, and T. Haraguchi, *Molecular communication.* Cambridge Univ. Press, Sep. 2013.

[3] L. Felicetti, M. Femminella, G. Reali, and P. Liò, "Applications of molecular communications to medicine: A survey," *Nano Commun. Netw.*, vol. 7, pp. 27–45, Mar. 2016.

[4] I. F. Akyildiz, M. Pierobon, S. Balasubramaniam, and Y. Koucheryavy, "The Internet of Bio-Nano Things," *IEEE Commun. Mag.*, vol. 53, no. 3, pp. 32–40, Mar. 2015.

[5] D. Malak and O. B. Akan, "Molecular communication nanonetworks inside human body," *Nano Commun. Netw.*, vol. 3, no. 1, pp. 19–35, Mar. 2012.

[6] C. A. Söldner *et al.*, "A survey of biological building blocks for synthetic molecular communication systems," *IEEE Commun. Surv. Tut.*, vol. 22, no. 4, pp. 2765–2800, Jul. 2020.

[7] R. A. Dixon and C. J. Lamb, "Molecular communication in interactions between plants and microbial pathogens," *Annu. Rev. Plant Biol.*, vol. 41, no. Volume 41, 1990, pp. 339–367, 1990.

[8] T. Nakano, M. J. Moore, F. Wei, A. V. Vasilakos, and J. Shuai, "Molecular communication and networking: Opportunities and challenges," *IEEE Trans. NanoBiosci.*, vol. 11, no. 2, pp. 135–148, May 2012.

[9] N. Farsad, H. B. Yilmaz, A. Eckford, C.-B. Chae, and W. Guo, "A comprehensive survey of recent advancements in molecular communication," *IEEE Commun. Surv. Tut.*, vol. 18, no. 3, pp. 1887–1919, Feb. 2016.

[10] V. Jamali, A. Ahmadzadeh, W. Wicke, A. Noel, and R. Schober, "Channel modeling for diffusive molecular communication - A tutorial review," *Proc. IEEE*, vol. 107, no. 7, pp. 1256–1301, Jun. 2019.

[11] M. Kuscu, E. Dinc, B. A. Bilgin, H. Ramezani, and O. B. Akan, "Transmitter and receiver architectures for molecular communications: A survey on physical design with modulation, coding, and detection techniques," *Proc. IEEE*, vol. 107, no. 7, pp. 1302–1341, May 2019.

[12] M. Ş. Kuran, H. B. Yilmaz, I. Demirkol, N. Farsad, and A. Goldsmith, "A survey on modulation techniques in molecular communication via diffusion," *IEEE Commun. Surv. Tut.*, vol. 23, no. 1, pp. 7–28, Dec. 2020.

[13] S. Lotter *et al.*, "Experimental research in synthetic molecular communications – Part I," *IEEE Nanotechnol. Mag.*, vol. 17, no. 3, pp. 42–53, Apr. 2023.

[14] ——, "Experimental research in synthetic molecular communications – Part II," *IEEE Nanotechnol. Mag.*, vol. 17, no. 3, pp. 54–65, Apr. 2023.

[15] M. Bartunik, G. Fischer, and J. Kirchner, "The development of a biocompatible testbed for molecular communication with magnetic nanoparticles," *IEEE Trans. Mol. Biol. Multi-Scale Commun.*, vol. 9, no. 2, pp. 179–190, Jun. 2023.

[16] L. Lin, W. Wang, W. Yu, and H. Yan, "Testbed for molecular communication system based on light absorption: Study of information transmission from inside to outside body," *IEEE Trans. Mol. Biol. Multi-Scale Commun.*, vol. 10, no. 2, Jun. 2024.

[17] J. Wang, D. Hu, C. Shetty, and H. Hassanieh, "Understanding and embracing the complexities of the molecular communication channel in liquids," in *Proc. Annu. Int. Conf. Mobile Comput.*, Sep. 2020, pp. 1–15.

[18] A. Wietfeld, S. Schmidt, and W. Kellerer, "Evaluation of a multi-molecule molecular communication testbed based on spectral sensing," *arXiv version arXiv:2405.10280*, May 2024.

[19] S. Angerbauer *et al.*, "Salinity-based molecular communication in microfluidic channels," *IEEE Trans. Mol. Biol. Multi-Scale Commun.*, vol. 9, no. 2, pp. 191–206, Jun. 2023.

[20] N. Farsad, D. Pan, and A. Goldsmith, "A novel experimental platform for in-vessel multi-chemical molecular communications," in *Proc. IEEE Global Commun. Conf.*, Dec. 2017, pp. 1–6.

[21] V. Walter, D. Bi, A. Salehi-Reyhani, and Y. Deng, "Real-time signal processing via chemical reactions for a microfluidic molecular communication system," *Nat. Commun.*, vol. 14, no. 1, p. 7188, Nov. 2023.

[22] N. Tuccitto, G. Li-Destri, G. M. Messina, and G. Marletta, "Fluorescent quantum dots make feasible long-range transmission of molecular bits," *J. Phys. Chem. Lett.*, vol. 8, no. 16, pp. 3861–3866, Aug. 2017.

[23] M. Schäfer *et al.*, "The Chorioallantoic Membrane model: A 3D in vivo testbed for design and analysis of MC systems," in *Proc. Int. Conf. Nanosc. Comput. Commun.*, Jun. 2024, pp. 47–53.

[24] L. Brand *et al.*, "Media modulation based molecular communication," *IEEE Trans. Commun.*, vol. 70, no. 11, pp. 7207–7223, Sep. 2022.

[25] ——, "Switchable signaling molecules for media modulation: Fundamentals, applications, and research directions," *IEEE Commun. Mag.*, pp. 1–7, Sep. 2023.

[26] H. A. Richards, C.-T. Han, R. G. Hopkins, M. L. Failla, W. W. Ward, and C. N. Stewart Jr, "Safety assessment of recombinant green fluorescent protein orally administered to weaned rats," *J. Nutr.*, vol. 133, no. 6, pp. 1909–1912, Jun. 2003.

[27] T. Brakemann *et al.*, "A reversibly photoswitchable GFP-like protein with fluorescence excitation decoupled from switching," *Nat. Biotechnol.*, vol. 29, no. 10, pp. 942–947, Sep. 2011.

[28] L. Lin, J. Zhang, M. Ma, and H. Yan, "Time synchronization for molecular communication with drift," *IEEE Commun. Lett.*, vol. 21, no. 3, pp. 476–479, Mar. 2016.

[29] V. Jamali, A. Ahmadzadeh, and R. Schober, "Symbol synchronization for diffusion-based molecular communications," *IEEE Trans. NanoBiosci.*, vol. 16, no. 8, pp. 873–887, Dec. 2017.

[30] X. Qian, S. Angerbauer, M. Egan, M. D. Renzo, and W. Haselmayr, "A molecular communication perspective on synchronization of coupled microfluidic-spectroscopy," *IEEE Trans. NanoBiosci.*, vol. 23, no. 3, pp. 458–471, Apr. 2024.

[31] L. Y. Debus, P. Hofmann, J. Torres Gómez, F. H. P. Fitzek, and F. Dressler, "Synchronized relaying in molecular communication: An AI-based approach using a mobile testbed setup," *IEEE Trans. Mol. Biol. Multi-Scale Commun.*, vol. 10, no. 3, pp. 470–475, Jun. 2024.

[32] L. Khaloopour *et al.*, "An experimental platform for macro-scale fluidic medium molecular communication," *IEEE Trans. Mol. Biol. Multi-Scale Commun.*, vol. 5, no. 3, pp. 163–175, Dec. 2019.

[33] M. Kuscu, H. Ramezani, E. Dinc, S. Akhavan, and O. B. Akan, "Fabrication and microfluidic analysis of graphene-based molecular communication receiver for Internet of Nano Things (IoNT)," *Sci. Rep.*, vol. 11, no. 1, p. 19600, Oct. 2021.

[34] M. Scherer *et al.*, "Closed-loop long-term experimental molecular communication system," *Zenodo*, 2024, DOI: 10.5281/zenodo.13898880. [Online]. Available: https://zenodo.org/uploads/13898880

[35] S. Wang, X. Chen, L. Chang, R. Xue, H. Duan, and Y. Sun, "GMars-Q enables long-term live-cell parallelized reversible saturable optical fluorescence transitions nanoscopy," *ACS Nano*, vol. 10, no. 10, pp. 9136–9144, Aug. 2016.

[36] R. Darby and R. P. Chhabra, *Chemical Engineering Fluid Mechanics*. Boca Raton, FL, USA: Taylor & Francis, 2016.

[37] H. Schlichting and K. Gersten, *Boundary-layer Theory*. Berlin/Heidelberg, Germany: Springer, 2016.

[38] M. A. Hink *et al.*, "Structural dynamics of green fluorescent protein alone and fused with a single chain Fv protein," *J. Biol. Chem.*, vol. 275, no. 23, pp. 17 556–17 560, Jun. 2000.

[39] C. G. Caro, *The Mechanics of the Circulation*. Cambridge, England: Cambridge University Press, 2012.

[40] P. Tabeling, *Introduction to Microfluidics*. Oxford, England: Oxford University Press, 2023.

[41] C. Junghans, F.-J. Schmitt, V. Vukojević, and T. Friedrich, "Diffusion behavior of the fluorescent proteins eGFP and Dreiklang in solvents of different viscosity monitored by fluorescence correlation spectroscopy," *Optofluid. Microfluid. Nanofluid.*, vol. 3, Jan. 2016.

[42] L. Grebenstein *et al.*, "Biological optical-to-chemical signal conversion interface: A small-scale modulator for molecular communications," in *Proc. Int. Conf. Nanosc. Comput. Commun.*, Sep. 2018, pp. 1–6.

[43] L. Mandel, "Fluctuations of photon beams: The distribution of the photo-electrons," *Proc. Phys. Soc.*, vol. 74, no. 3, p. 233, Apr. 1959.

[44] W. S. Cleveland and S. J. Devlin, "Locally weighted regression: An approach to regression analysis by local fitting," *J. Am. Stat. Assoc.*, vol. 83, no. 403, pp. 596–610, Sep. 1988.

[45] J. G. Proakis, *Digital communications*. New York, NY, USA: McGraw-Hill, Higher Education, 2008, vol. 5th ed.

[46] B.-H. Koo, H. J. Kim, J.-Y. Kwon, and C.-B. Chae, "Deep learning-based human implantable nano molecular communications," in *Proc. IEEE Int. Conf. Commun.*, Jul. 2020, pp. 1–7.

[47] M. Bartunik, M. Streb, H. Unterweger, J. Haller, and J. Kirchner, "Increasing the channel capacity: Parallel data transmission in a testbed for molecular communication," in *Proc. Int. Conf. Nanosc. Comput. Commun.*, 2021, pp. 1–6.

[48] Y. Huang, X. Huang, F. Ji, M. Cheng, X. Chen, and M. Wen, "A non-invasive and high-speed molecular communication testbed with capacitive sensing," in *IEEE Conf. Comp. Commun. Work.*, May 2024, pp. 1–2.

ACKNOWLEDGMENT